Review

Chenglong You*, Apurv Chaitanya Nellikka, Israel De Leon and Omar S. Magaña-Loaiza

Multiparticle quantum plasmonics

https://doi.org/10.1515/nanoph-2019-0517
Received December 13, 2019; revised February 18, 2020; accepted March 4, 2020

Abstract: A single photon can be coupled to collective charge oscillations at the interfaces between metals and dielectrics forming a single surface plasmon. The electromagnetic near-fields induced by single surface plasmons offer new degrees of freedom to perform an exquisite control of complex quantum dynamics. Remarkably, the control of quantum systems represents one of the most significant challenges in the field of quantum photonics. Recently, there has been an enormous interest in using plasmonic systems to control multiphoton dynamics in complex photonic circuits. In this review, we discuss recent advances that unveil novel routes to control multiparticle quantum systems composed of multiple photons and plasmons. We describe important properties that characterize optical multiparticle systems such as their statistical quantum fluctuations and correlations. In this regard, we discuss the role that photon-plasmon interactions play in the manipulation of these fundamental properties for multiparticle systems. We also review recent works that show novel platforms to manipulate many-body light-matter interactions. In this spirit, the foundations that will allow nonexperts to understand new perspectives in multiparticle quantum plasmonics are described. First, we discuss the quantum statistical fluctuations of the electromagnetic field as well as the fundamentals of plasmonics and its quantum properties. This discussion is followed by a brief treatment of the dynamics that characterize complex multiparticle interactions. We apply these ideas to describe quantum interactions in photonic-plasmonic multiparticle quantum systems. We summarize the state-of-the-art in quantum devices that rely on plasmonic interactions. The review is concluded with our perspective on the future applications and challenges in this burgeoning field.

Keywords: quantum plasmonics; nonclassical states of light; multiparticle interactions; nanophotonics; near-field effects; surface plasmons.

1 Introduction

Plasmonics studies the science and applications of surface plasmon polaritons (SPPs), which are coupled excitations comprising a charge density wave at the surface of a metal and an electromagnetic field. SPPs are optical surface waves that can propagate along the interface between a metal and a dielectric. These surface waves can also exist in metallic nanoparticles, where they take the form of standing excitations localized to the nanoparticle and are referred to as localized surface plasmons (LSPs). The remarkable properties of plasmonic systems, such as subwavelength field confinement [1, 2], large field enhancement [3–5], and large sensitivity to the surrounding environment [6–9], have been exploited for a variety of applications, including biochemical sensing, nanoscopic lasers, nonlinear nanophotonic devices, and optical metamaterials [10–19]. Surface plasmons (as we will refer collectively to as both SPPs and LSPs) behave similar to bosons, and their classical properties can be described by Maxwell's equations with the appropriate boundary conditions. However, their intriguing quantum properties are revealed, for instance, when the coupled excitation occurs at the single-photon level [20] or in metallic nanostructures whose dimensions lead to quantum behavior of the charge density through quantum size effects [21–23].

Recently, there have been efforts to achieve a new degree of control of quantum systems through the manipulation of electromagnetic near-fields via surface plasmons [24–26]. The advancement in fabrication techniques and the availability of powerful computers for simulation have enabled strong light confinement to induce novel light-matter interactions, in nanostructures, which cannot be achieved in traditional free-space quantum optics [1, 2, 12, 27–29]. This kind of platforms offers the possibility of using near-field effects to control scattering processes,

***Corresponding author: Chenglong You,** Quantum Photonics Laboratory, Department of Physics and Astronomy, Louisiana State University, Baton Rouge, LA 70803, USA, e-mail: yclong001@gmail.com. https://ocrid.org/0000-0002-1383-0551
Apurv Chaitanya Nellikka and Israel De Leon: School of Engineering and Sciences, Tecnológico de Monterrey, Monterrey, Nuevo Leon 64849, Mexico
Omar S. Magaña-Loaiza: Quantum Photonics Laboratory, Department of Physics and Astronomy, Louisiana State University, Baton Rouge, LA 70803, USA

coherence, the propagation direction of light, and exotic light-matter interactions at the level of a single particle [30–33]. Although surface plasmons are known to suffer from losses, the underlying scattering processes among photons and plasmons provide additional quantum interference paths that can be used to control quantum mechanical systems. Indeed, the lossy nature of surface plasmons offers additional mechanisms for controlling dissipative dynamics behind decoherence. These possibilities have opened up new research directions in which the quantum properties of plasmons are used to manipulate many-body systems of photons in applications ranging from quantum sensing to quantum networks [1, 2, 12, 27, 33–41].

We start our review with a discussion on the quantum properties of photonic and plasmonic systems. In Sections 2 and 3, we describe the quantum properties of plasmonic fields that have been used to control multiparticle systems. In Section 4, we review the recent findings related to the preservation of quantum statistics in plasmonic systems. We then discuss recent progress on quantum control through the use of electromagnetic near-fields in Section 5. A review of quantum hybrid devices that use nonclassical evanescent near-fields will be presented in Section 6. Finally, we conclude our review by providing the reader with the most representative challenges in the field of multiparticle quantum plasmonics.

2 Fundamentals of quantum optics

2.1 Quantum properties of the electromagnetic field

In this section, we review the quantization of Maxwell's equations. The reader can find additional discussions and details in Refs. [42–45]. Our treatment assumes the absence of sources of radiation and vacuum propagation only, where Maxwell's equations read as

$$\begin{aligned} \nabla\times\mathbf{E} &= -\frac{\partial\mathbf{B}}{\partial t}, \\ \nabla\times\mathbf{B} &= \frac{1}{c^2}\frac{\partial\mathbf{E}}{\partial t}, \\ \nabla\cdot\mathbf{B} &= 0, \\ \nabla\cdot\mathbf{E} &= 0. \end{aligned} \tag{1}$$

Here, c is the speed of light in vacuum and $\mathbf{E}$ and $\mathbf{B}$ represent the electric and magnetic fields, respectively.

Then considering a one-dimensional cavity of length L with perfectly conducting walls, we obtain the single-mode field solution,

$$E_x(z,t)=\sqrt{\frac{2\omega^2}{V\varepsilon_0}}Q(t)\sin(kz), \tag{2}$$

where we have taken the wave's propagation along the z direction and polarization along the x direction. Moreover, V represents the effective volume of the cavity and $Q(t)$ defines a canonical position. In addition, here k and ω are the wavenumber and frequency of the mode, respectively. As the one-dimensional boundary condition must be met, where $k=j\pi/L(j=1, 2, 3, \ldots)$, the magnetic field in the cavity is

$$B_y(z,t)=\frac{1}{c^2}\sqrt{\frac{2\omega^2}{V\varepsilon_0}}\frac{\dot{Q}(t)}{k}\cos(kz). \tag{3}$$

Then, the classical field energy of the single-mode field, i.e. the Hamiltonian H, is given by

$$H=\frac{1}{2}\int\left(\frac{1}{\mu_0}\mathbf{B}^2+\varepsilon_0\mathbf{E}^2\right)dV=\frac{1}{2}(p^2+\omega^2q^2), \tag{4}$$

where $p=\dot{q}$; these are canonical variables for classical systems. Then, it is clear that the single-mode field is equivalent to a harmonic oscillator of unit mass. To quantize the single-mode field, one can then introduce the canonical commutation relation,

$$[\hat{q},\hat{p}]=i\hbar, \tag{5}$$

where $\hbar=h/2\pi$. Then, by convention, we introduce the annihilation $\hat{a}$ and creation $\hat{a}^\dagger$ operators

$$\hat{a}=\sqrt{\frac{1}{2\hbar\omega}}(\omega\hat{q}+i\hat{p}), \tag{6}$$

$$\hat{a}^\dagger=\sqrt{\frac{1}{2\hbar\omega}}(\omega\hat{q}-i\hat{p}). \tag{7}$$

The annihilation operator $\hat{a}$ and the creation operator $\hat{a}^\dagger$ satisfy the commutation relation

$$[\hat{a},\hat{a}^\dagger]=1. \tag{8}$$

Therefore, the Hamiltonian can be written as

$$\hat{H}=\hbar\omega\left(\hat{a}^\dagger\hat{a}+\frac{1}{2}\right). \tag{9}$$

This description enables us to quantize the electromagnetic field.

2.2 Quantum states of light

The annihilation and creation operators can be used to describe quantum states of light. Remarkable examples include Fock states, coherent states, squeezed states, and thermal states. The possibility of preparing light in these states has been extensively used to prepare many-body systems of photons.

2.2.1 Fock states

We will start this section by describing a particular family of nonclassical states of light known as Fock or photon number states. These are eigenstates of the Hamiltonian $\hat{H}$, and we denote them as $|n\rangle$. In this case, n represents the number of photons in a single mode of the electromagnetic field. Interestingly, Fock states have a well-defined number of particles. Thus, we can define the particle number operator as $\hat{n}=\hat{a}^{\dagger}\hat{a}$, which satisfies

$$\hat{n}|n\rangle = n|n\rangle. \tag{10}$$

Moreover, the action of the creation and annihilation operators on the Fock state $|n\rangle$ is given by

$$\hat{a}^{\dagger}|n\rangle = \sqrt{n+1}\,|n+1\rangle, \tag{11}$$

$$\hat{a}|n\rangle = \sqrt{n}\,|n-1\rangle. \tag{12}$$

The number state $|n\rangle$ can be obtained from the vacuum state $|0\rangle$ as

$$|n\rangle = \frac{(\hat{a}^{\dagger})^n}{\sqrt{n!}}|0\rangle. \tag{13}$$

From Eq. (13), we can also derive some properties of these quantum states. Fock states are orthonormal:

$$\langle n|m\rangle = \delta_{nm}, \tag{14}$$

and the Fock state basis is complete

$$\sum_{n=0}^{\infty}|n\rangle\langle n| = \hat{I}. \tag{15}$$

2.2.2 Coherent states

Coherent states can be used to describe photons in an ideal laser beam. These are quantum mechanical states with classical noise properties [42]. The definition of a coherent state $|\alpha\rangle$ is given by the annihilation operator

$$\hat{a}|\alpha\rangle = \alpha|\alpha\rangle. \tag{16}$$

Therefore, a coherent state is an eigenstate of the annihilation operator. Similarly to Fock states, coherent states form a complete set of basis. Thus, one can represent coherent states in the number basis as

$$|\alpha\rangle = \exp\left(-\frac{1}{2}|\alpha|^2\right)\sum_{n=0}^{\infty}\frac{\alpha^n}{\sqrt{n!}}|n\rangle. \tag{17}$$

It is worth noting that coherent states do not have a definite photon number. Rather, their photon number follows a Poissonian statistical distribution,

$$P(n) = e^{-|\alpha|^2}\frac{|\alpha|^{2n}}{n!}, \tag{18}$$

with standard deviation of $\Delta n = |\alpha| = \sqrt{\langle n\rangle}$. Hence, the average photon number of coherent states is

$$\langle\hat{n}\rangle = \langle\alpha|\hat{a}^{\dagger}\hat{a}|\alpha\rangle = |\alpha|^2. \tag{19}$$

Moreover, coherent states have equal uncertainties in both quadratures $\hat{X}_1$ and $\hat{X}_2$, where

$$\langle(\Delta\hat{X}_1)^2\rangle = \langle(\Delta\hat{X}_2)^2\rangle = \frac{1}{4}. \tag{20}$$

Here, $\hat{X}_1$ and $\hat{X}_2$ are defined as

$$\hat{X}_1 = \frac{\hat{a}+\hat{a}^{\dagger}}{2}, \tag{21}$$

$$\hat{X}_2 = \frac{\hat{a}-\hat{a}^{\dagger}}{2i}. \tag{22}$$

2.2.3 Squeezed states

Squeezed states represent an important family of nonclassical states that have been extensively used for quantum sensing [46–52]. This is due to the possibility of reducing quadrature fluctuations beyond those that characterize states with classical noise properties [53]. Generally, squeezed states can be generated through parametric

processes in nonlinear materials, including parametric down-conversion (PDC) [54] and four-wave mixing [55]. For sake of completeness, we describe single-mode squeezed vacuum states, which could be expanded in the Fock state basis as

$$|0,\xi\rangle = \frac{1}{\sqrt{\cosh r}} \sum_{n=0}^{\infty} \frac{\sqrt{(2n)!}}{n!} \left(-\frac{1}{2} e^{i\theta} \tanh r \right)^n |2n\rangle, \tag{23}$$

where r is the squeezing parameter and θ represents the angle in the quadrature space. Another relevant squeezed state is the two-mode squeezed vacuum (TMSV) state, which is given by

$$|\xi\rangle_{ab} = \frac{1}{\cosh r} \sum_{n=0}^{\infty} (-1)^n e^{i\theta} \tanh^n r \, |n,n\rangle_{ab}. \tag{24}$$

The average photon number in each mode of the TMSV state is given by

$$\langle \hat{n}_a \rangle = \langle \hat{n}_b \rangle = \sinh^2 r. \tag{25}$$

Furthermore, the photon number fluctuations of TMSV states can be described as

$$\langle (\Delta \hat{n}_a)^2 \rangle = \langle (\Delta \hat{n}_b)^2 \rangle = \frac{1}{4} \sinh^2(2r), \tag{26}$$

consequently, both modes of TMSV states exhibit super-Poissonian photon statistics.

TMSV states cannot be written as the product of states describing photons in modes a and b. Instead, these states exhibit nonclassical correlations between the two modes. We can see in Eq. (24) that photons in the two modes show perfect photon-number correlations and are entangled. As described below, these unique properties have been used in photonic and plasmonic systems. If the squeezing r is weak, then the prominent terms in Eq. (24) are vacuum state $|00\rangle_{ab}$ and the biphoton state $|11\rangle_{ab}$. For this reason, TMSV states have been used as single-photon sources, where one mode is used as a heralding mode, whereas the other mode is used as the source of single photons.

2.2.4 Thermal state

Now, we will focus our attention to the description of thermal states. This family of states describes common light sources such as sunlight. These sources of light are characterized by classical noise properties that can be mathematically described by statistical mixtures of number states as

$$\hat{\rho}_{\text{th}} = \frac{\bar{n}}{1+\bar{n}} \sum_{n=0}^{\infty} \left(\frac{\bar{n}}{1+\bar{n}} \right)^n |n\rangle\langle n|. \tag{27}$$

Here, $\bar{n}$ represents the mean photon number of the thermal field. Furthermore, the photon number fluctuations of the thermal state can be described as

$$\langle (\Delta n)^2 \rangle = \langle \hat{n}^2 \rangle - \langle \hat{n} \rangle^2 = \bar{n} + \bar{n}^2, \tag{28}$$

which is larger than the mean photon number $\bar{n}$. Thus, thermal states show super-Poissonian photon statistics.

2.3 Classical and quantum coherence

The advent of the laser gave an enormous impulse to the development of the theory of optical coherence [56]. Nowadays, photonic technologies depend to an important extent on our ability to manipulate the coherence properties of the electromagnetic field. In this regard, plasmonic systems have been extensively used to engineer the spatial and temporal properties of photons. In this section, we provide a brief review of the concept of spatial coherence, a property that will be used in several parts of this review. We illustrate this concept through the famous Young's two-slit experiment (see Figure 1).

The double-slit experiment was introduced by Thomas Young to illustrate the wave nature of light. This beautiful experiment has also been used to quantify spatial coherence of light. We show a simplified version of this experiment in Figure 1. We assume that a double-slit structure is illuminated with a quasi-monochromatic source of light.

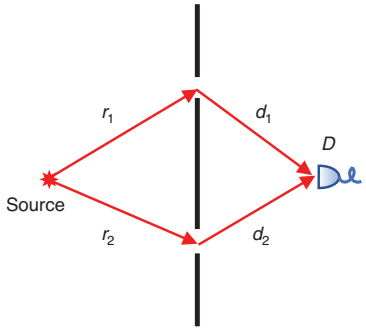

Figure 1: Schematic of Young's double-slit setup. Here, r_1 and r_2 represent the distances from the source to the upper and lower slits, respectively. The distances from the upper and lower slits to the detector D are represented by d_1 and d_2, respectively.

At time t, the total electric field at the detector $E_d(r, t)$ is given by

$$E_d(r, t) = a_1 E(r_1, t_1) e^{ik_0 d_1} + a_2 E(r_2, t_2) e^{ik_0 d_2}, \tag{29}$$

which is the sum of the field amplitudes $E(r_1, t_1)$ and $E(r_2, t_2)$ produced by each of the slits. Here, $t_1 = t - d_1/c$ and $t_2 = t - d_2/c$ represent the times at which the photons leave the slits, and $k_0 = \omega/c$ is the wavenumber in vacuum. The values for a_1 and a_2 are defined by the geometry of the slits. Then, the intensity I_d measured by the detector D is given by

$$\begin{aligned} I_d(r) &= \langle E_d^{\star}(r, t) E_d(r, t) \rangle \\ &= a_1^2 I_1(r_1, t_1) + a_2^2 I_2(r_2, t_2) \\ &\quad + a_1 a_2 \Gamma(r_1, r_2, t_1, t_2) e^{-ik_0(d_1 - d_2)} + c.c., \end{aligned} \tag{30}$$

where $I_1 = \langle E^*(r_1, t_1) E(r_1, t_1) \rangle$ and $I_2 = \langle E^*(r_2, t_2) E(r_2, t_2) \rangle$. The notation $\langle \cdots \rangle$ represents an ensemble average. These quantities can be used to introduce the mutual coherence function

$$\Gamma^{(1)}(r_1, r_2, t_1, t_2) = \langle E^*(r_1, t_1) E(r_2, t_2) \rangle. \tag{31}$$

Indeed, it is possible to express Eq. (30) as

$$\begin{aligned} I_d(r) &= \langle E_d^{\star}(r, t) E_d(r, t) \rangle \\ &= a_1^2 I_1(r_1, t_1) + a_2^2 I_2(r_2, t_2) + 2 |a_1| |a_2| Re[\Gamma(r_1, r_2, t_1, t_2)]. \end{aligned} \tag{32}$$

The first two terms in Eq. (32) are transmission contributions from the first and second slits, respectively. Furthermore, the last term in Eq. (32) describes interference. The intensities $I_1(r_1, t_1)$ and $I_2(r_2, t_2)$ provide information about self-field correlations. These can be described by the functions of first-order coherence $\Gamma^{(1)}(r_1, r_1, t_1, t_1)$ and $\Gamma^{(1)}(r_2, r_2, t_2, t_2)$. Similarly, the mutual-field correlations can be described by the function of first-order coherence $\Gamma^{(1)}(r_1, r_2, t_1, t_2)$. It is worth noting that the interference fringes are formed when the length of the spatial coherence of the illuminating beam is larger than the separation between the slits. In other words, interference fringes are produced when the properties of light are similar at the spatial locations defined by the two slits. The quality of the formed fringes can be quantified through Rayleigh's definition of fringe visibility,

$$\mathcal{V} = (I_{max} - I_{min}) / (I_{max} + I_{min}), \tag{33}$$

where I_{max} and I_{min} are the maximum and minimum intensity values in the interference pattern, respectively. The visibility $\mathcal{V}$ is equal to zero for incoherent sources. Furthermore, $\mathcal{V} = 1$ describes a coherent source. Also, sources of light characterized by visibilities in the range $0 \le \mathcal{V} \le 1$ are considered partially coherent.

A quantum formulation of coherence can be constructed using similar ideas to those described above. In this regard, we introduce the general first-order correlation function [42, 44, 45],

$$G^{(1)}(r_1, r_2, t_1, t_2) = Tr\{\hat{\rho} \hat{E}^{(-)}(r_1, t_1) \hat{E}^{(+)}(r_2, t_2)\}, \tag{34}$$

where $\hat{\rho}$ is the density matrix of a quantum state, and $\hat{E}^{(+)}$ is the electric-field operator and $\hat{E}^{(-)} = [\hat{E}^{(+)}]^{\dagger}$. In addition, the normalized first-order correlation function is defined as

$$g^{(1)}(r_1, r_2, t_1, t_2) = \frac{G^{(1)}(r_1, r_2, t_1, t_2)}{[G^{(1)}(r_1, r_1, t_1, t_1) G^{(1)}(r_2, r_2, t_2, t_2)]^{1/2}}. \tag{35}$$

As discussed above, the first-order coherence function can be used to determine the spatial coherence of the electromagnetic field. However, additional information can be gained through the implementation of intensity correlations. In this regard, in 1956, Hanbury Brown and Twiss (HBT) performed a novel interference experiment through the use of measurements of intensity correlation [57]. The original HBT stellar interferometer was designed to determine diameters of stars [58]. This experiment used two detectors located at different positions on Earth that collected light produced by independent sources on the disc of a star.

A simplified schematic of the HBT experiment is shown in Figure 2. Here, two detectors D_1 and D_2 are placed at the same distance from the beam splitter. The setup measures intensity correlations as a function of the time delay between the signals generated by the two detectors. Here, the coincident count rate is given by

$$C(t_1, t_2) = \langle I(t_1) I(t_2) \rangle, \tag{36}$$

where $I(t_1)$ and $I(t_2)$ are the intensities measured by the two detectors D_1 and D_2. The generic function for second-order coherence is defined as

$$\Gamma^{(2)}(t_1, t_2) = \langle E^*(t_1) E(t_1) E^*(t_2) E(t_2) \rangle \tag{37}$$

which describes a statistical average of the product of intensities associated to the fields $E(t_1)$ and $E(t_2)$. In general, the fields are detected at two different spatial and temporal positions. For practical purposes, we use the normalized version of the classical second-order coherence function

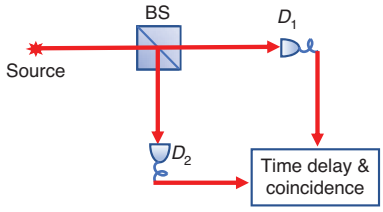

Figure 2: Diagram of the HBT interferometer.
A pseudothermal beam of light is passed through a beam splitter (BS) and measured by two detectors D_1 and D_2. The time delay between the two detectors is controlled in this experiment, and the output signals produced by both detectors are correlated. This measurement is equivalent to the implementation of correlations of intensity fluctuations.

$$\gamma^{(2)}(\tau)=\frac{\langle E^*(t_1)E(t_1)E^*(t_2)E(t_2)\rangle}{\langle E^*(t_1)E(t_1)\rangle^2}, \tag{38}$$

where $\tau=t_1-t_2$ is the time delay between the two light beams, and it is smaller than the coherence time of the source.

Similar to the first-order quantum coherence function, we can introduce the second-order quantum coherence function [42, 44, 45],

$$G^{(2)}(t_1, t_2; t_2, t_1)=Tr\{\hat{\rho}\hat{E}^{(-)}(t_1)\hat{E}^{(-)}(t_2)\hat{E}^{(+)}(t_2)\hat{E}^{(+)}(t_1)\}, \tag{39}$$

and the normalized second-order quantum coherence function, $g^{(2)}$, is given by

$$g^{(2)}(t_1, t_2; t_2, t_1)=\frac{G^{(2)}(t_1, t_2; t_2, t_1)}{G^{(1)}(t_1, t_1)G^{(1)}(t_2, t_2)}. \tag{40}$$

Notably, for a single-mode field, it is possible to reduce Eq. (40) to

$$g^{(2)}(\tau)=1+\frac{\langle(\Delta\hat{n})^2\rangle-\langle\hat{n}\rangle}{\langle\hat{n}\rangle^2}. \tag{41}$$

We can observe that Eq. (41) does not depend on the time difference τ. The second-order quantum coherence function thus becomes a powerful tool to probe the underlying statistical properties of light.

It is worth noting the values of $g^{(2)}(0)$ for different light sources. For an attenuated laser, which is described by coherent states $|\alpha\rangle$, $g^{(2)}(0)=1$. Furthermore, a single-mode thermal state $\hat{\rho}_{th}$ is characterized by $g^{(2)}(0)=2$. Indeed, any classical electric field satisfies $g^{(2)}(0)\geq 1$. For photon number states (Fock states) represented by $|n\rangle$, for a situation in which $n\geq 1$, it can be shown that $g^{(2)}(0)=1-1/n$. Particularly, for a single-photon state $|1\rangle$, one expects $g^{(2)}(0)=0$. By comparing the aforementioned examples, we conclude that the measurement of $g^{(2)}$ can be used to characterize nonclassical properties of light [59]. Later in this review, we will discuss how recent work on quantum plasmonic relies on the measurements of first- and second-order quantum coherence.

2.4 Hong, Ou, and Mandel (HOM) interference

In 1987, Hong, Ou and Mandel, unveiled the fundamental physics behind bosonic interference through an emblematic experiment that cannot be explained using the classical theory of light [60]. As illustrated in Figure 3, in this experiment, two indistinguishable photons are injected into the input ports of a beam splitter. The pair of photons is described by the state $|1, 1\rangle_{in}=\hat{a}_{in}^{\dagger}\hat{b}_{in}^{\dagger}|0, 0\rangle_{in}$, where $\hat{a}_{in}^{\dagger}$ and $\hat{b}_{in}^{\dagger}$ denote the two modes of the injected photons. Following the transformation of a 50/50 beam splitter, we have

$$\begin{aligned}|1,1\rangle_{in} &\xrightarrow{BS}\frac{1}{2}(\hat{a}_{out}^{\dagger}+i\hat{b}_{out}^{\dagger})(i\hat{a}_{out}^{\dagger}+\hat{b}_{out}^{\dagger})|0, 0\rangle_{out}\\ &=\frac{i}{2}(\hat{a}_{out}^{\dagger}\hat{a}_{out}^{\dagger}+\hat{b}_{out}^{\dagger}\hat{b}_{out}^{\dagger})|0, 0\rangle_{out}\\ &=\frac{i}{\sqrt{2}}(|2, 0\rangle_{out}+|0, 2\rangle_{out}).\end{aligned} \tag{42}$$

According to Eq. (42), the two interfering photons are expected to emerge through the same output port of the beam splitter if these were simultaneously injected. Thus, one should observe photon bunching and the absence of simultaneous photon events. It is worth noting that the

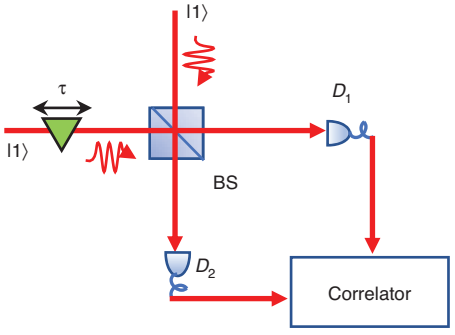

Figure 3: Schematic representation of the HOM two-photon interference experiment.
Two single photons with a relative time delay τ are injected into the input ports of a 50/50 beam splitter (BS) and measured by two detectors D_1 and D_2. The signals produced by the two detectors are analyzed using a correlation circuit.

bunching effect depends on the degree of indistinguishability of the interfering photons. In the famous HOM experiment, the single-photon pairs were generated through spontaneous PDC (SPDC) in a source with a spectral bandwidth $\Delta\omega$. In this case, the coincidence probability as a function of time delay τ is given by

$$P_{11} \propto 1-\exp(-\Delta\omega^2\tau^2). \tag{43}$$

At $\tau=0$, the two single photons are perfectly indistinguishable and the HOM dip is observed. Nowadays, the HOM experiment represents one of the basic tools to control multiphoton processes. In addition, it also serves as a platform to test indistinguishability among photons.

2.5 Quantum entanglement

Entanglement constitutes one of the most remarkable consequences of quantum mechanics. This interesting property of quantum mechanical systems was used as an argument to question the validity of quantum mechanics. Indeed, its origin can be traced back to 1935 when Einstein, Podolsky, and Rosen (EPR) pointed out its nonlocal nature [61]. The arguments presented by EPR aimed to demonstrate that quantum mechanics was an incomplete theory. In their seminal paper, EPR analyzed a system of two distant particles entangled simultaneously in their position and momentum properties. They pointed out that, in a system with these properties, one could perform a measurement of either position or momentum of one of the particles and infer, with complete certainty, either the position or the momentum, respectively, of the unmeasured particle. In their emblematic "gedanken" experiment, the two distant particles do not interact; thus, the possibility of inferring information of a distant particle would imply that the position and momentum of the unmeasured particle were simultaneous realities, leading to a violation of Heisenberg's uncertainty principle. Remarkably, over the past 25 years, a series of systematical experimental tests have demonstrated that entanglement is in fact a real property of quantum mechanical entities such as molecules, atoms, and photons [62–64].

Notably, SPDC offers the possibility of generating pairs of entangled photons optically [62, 63, 65]. As depicted in Figure 4, SPDC is a $\chi^{(2)}$ nonlinear process in which one pump photon is annihilated to generate entangled photon pairs [63]. In Figure 4B and C, linear momentum and energy are conserved in this nonlinear process. As shown in Figure 4A, a pair of entangled photons is generated at the same crystal position; consequently, the photons are correlated in the variable of linear position. In Figure 4A and B, the conservation of linear momentum forces the two beams to propagate with opposite spatial frequencies [67]. Thus, SPDC photons are characterized by opposite transverse wavevectors that induce anticorrelations in linear momentum. In Figure 4C, the energy conservation results in the wavelengths of the pump, signal, and idler photons satisfying $1/\lambda_p = 1/\lambda_s + 1/\lambda_i$. These conditions enable the generation of photons entangled in multiple degrees of freedom, such as in energy and time, angular position, and orbital angular momentum and polarization [68]. Below, we discuss experiments that rely on these forms of entanglement.

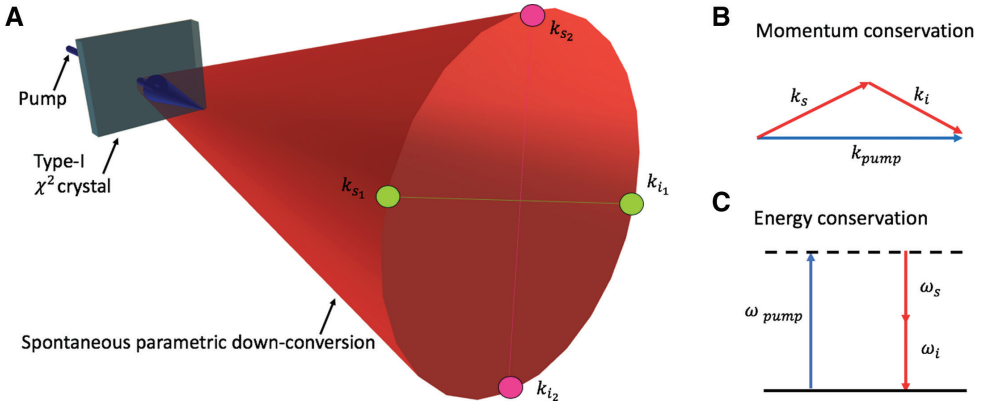

Figure 4: Spontaneous parametric down-conversion (SPDC) process and the conservation of momentum and energy.
(A) The process of SPDC is produced by pumping a $\chi^{(2)}$ nonlinear crystal. SPDC photons are generated at the same spatial position in the crystal; consequently, photon pairs are correlated in the variable of spatial position. The conservation of linear momentum shown in (B) forces a pair of SPDC photons to be anticorrelated in the variable of linear momentum; consequently, photons located in opposite positions of the down-conversion cone show nonclassical correlations. (C) The process of SPDC satisfies the conservation of energy; in this case, a blue photon is annihilated to create two red photons. Reproduced from Ref. [66].

3 Elements of plasmonics

3.1 Classical picture

As indicated earlier, surface plasmons are surface electromagnetic waves formed at the interface between a metal and a dielectric due to the interaction of surface charges and an electromagnetic field. These waves can propagate along the surface of a metal (SPPs) or can be localized to metallic nanoparticles (LSPs). For instance, consider the SPP of a single planar interface between a metal and a dielectric with permittivities, ε_m and ε_d, respectively, as shown in Figure 5A and B. Solving Maxwell's equations with the appropriate boundary conditions yields the following expression for the SPP wavenumber [69],

$$K = k_0\sqrt{\frac{\varepsilon_m\varepsilon_d}{\varepsilon_m+\varepsilon_d}}, \tag{44}$$

where $k_0=\omega/c$ is the magnitude of the wavevector in free space. K is a complex quantity because ε_m is generally a complex quantity. The real and imaginary parts of K can be approximated as

$$\begin{aligned} K' &\approx k_0\sqrt{\varepsilon'_m\varepsilon_d/\varepsilon'_m+\varepsilon_d}, \\ K'' &\approx k_0\sqrt{\varepsilon'_m\varepsilon_d/\varepsilon'_m+\varepsilon_d}\left[\frac{\varepsilon''_m\varepsilon_d}{2\varepsilon'_m(\varepsilon'_m+\varepsilon_d)}\right], \end{aligned} \tag{45}$$

where the prime and double prime symbols indicate real and imaginary parts, respectively. The approximation is valid when $|\varepsilon'_m|\ll|\varepsilon''_m|$, which is a reasonable approximation for noble metals in the visible and near-infrared

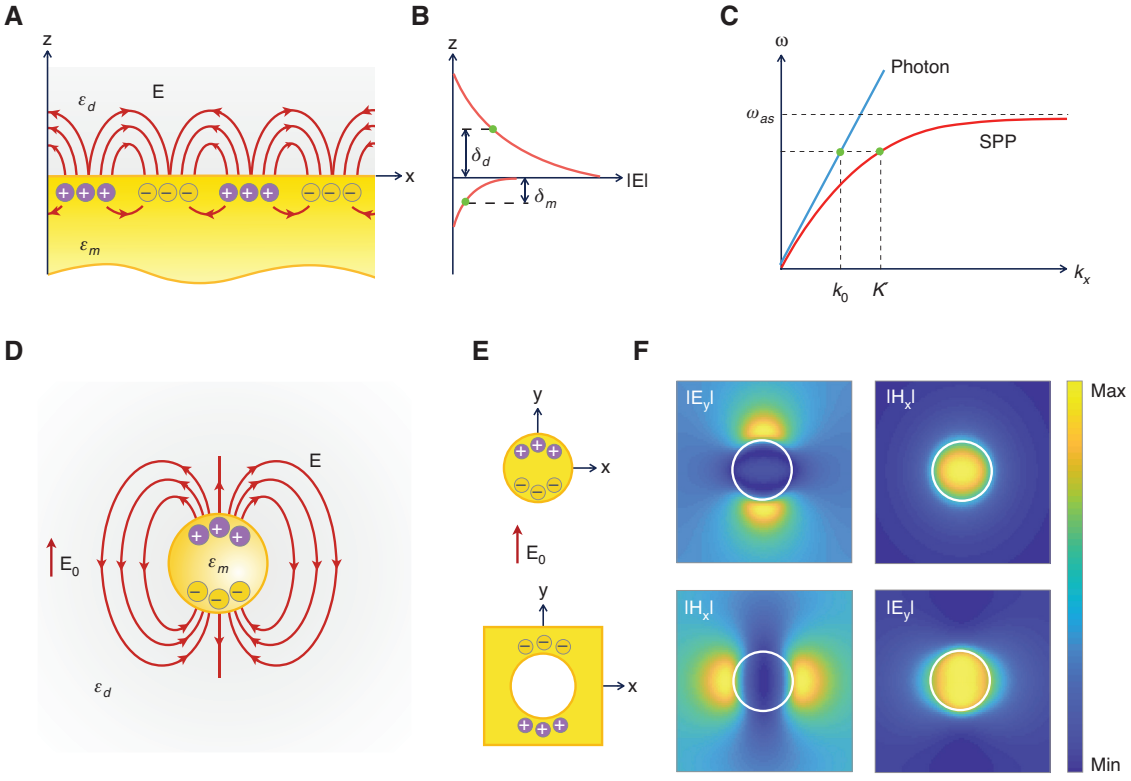

Figure 5: Electromagnetic properties of plasmonic structures.
(A) Illustration of the electric field lines and surface charge distribution associated with the SPP supported by a metal-dielectric interface. (B) Magnitude of the electric field across the interface showing the extend of electric field confinement. The penetration depth into the metal (δ_m) and dielectric (δ_d) characterize the SPP mode confinement. (C) Dispersion relations of SPPs (red line) and photons (blue line). The wavenumber of an SPP is larger than that of a photon in the dielectric medium and can acquire large values near the resonance frequency asymptote, ω_{as}. (D) Illustration of the electric field lines, E, associated with the LSP excited on a metallic nanosphere by an incident electric field, E_0. (E) Schematic illustration of the charge distribution in a metal disk (top) and a circular aperture (bottom) due to an incident electric field, E_0. (F) Calculated near-field distribution in the x, y-plane for a gold disk (top row) and a circular aperture (bottom row) having a diameter of 150 nm and a thickness of 30 nm. The calculations were carried out using the finite-difference time-domain method using a y-polarized plane wave excitation at a wavelength of 750 nm. The white circle indicates the position of the nanostructures.

region of the spectrum (away from interband transitions). The real part, K', is related to the phase evolution of the SPP and hence defines its dispersion relation (Figure 5C). The expression for K' predicts a significant increase in the SPP momentum at frequencies near the resonance-frequency asymptote ω_{as}, which is the frequency at which $\varepsilon_m' = -\varepsilon_d$, i.e. the frequency at which the denominator in Eq. (45) vanishes. Also, note that because of their surface-wave nature, SPPs possess wavenumbers that are larger than those of photons in the dielectric for a given frequency. Hence, momentum matching mechanisms, such as grating coupling or prism coupling, are required to excite them with photons. In contrast, the imaginary part K'' is associated with the SPP field attenuation, which limits the propagation range of the wave. The propagation length of the SPP is defined as the distance over which the field intensity is reduced by a factor of e^{-1} and is given by $\ell_{SPP} = 1/2K''$.

The SPP electric field is p-polarized [electric field oscillation confined to (z-x) plane] and its distribution has the form

$$\mathbf{E}_j = (E_{xj}, 0, E_{zj})\exp(i(Kx - \omega t))\exp(-k_{zj}z), \tag{46}$$

where the subindex $j \in \{m, d\}$ identifies the medium. Here, we have taken z as the direction normal to the metal-dielectric interface and x as the propagation direction. Note that the fields decay exponentially away from the interface and have their maximum amplitude right at the interface (Figure 5B). The degree of confinement to the metal-dielectric interface is determined by the penetration depth into the two media, $\delta_j = 1/k_{zj}$. Here, k_{zj} is the normal wavevector component in medium j and is given by

$$k_{zj} = k_0\sqrt{\frac{\varepsilon_j^2}{\varepsilon_m + \varepsilon_d}}. \tag{47}$$

Near the resonance-frequency asymptote, the magnitude of k_{zj} can be very large, resulting in a subwavelength mode confinement. The degree of mode confinement is only limited by the losses of the system, which increase significantly near the resonance-frequency asymptote.

Variants of this single-interface plasmonic structure described here may include metal films or stripes bounded by dielectrics [70, 71]. Such variants support SPP modes that share similar characteristics to the single-interface SPP discussed here. Nevertheless, the additional degrees of freedom associated with those structures allow them to support various modes with particular field symmetries [72–75].

For metallic nanoparticles with dimension smaller or comparable to the skin depth of the metal, the electric field can penetrate the nanoparticle and excite directly LSPs [69]. As these nanoparticles typically have dimensions much smaller than the wavelength, their electromagnetic response is well described by the first-order dipolar contribution. Furthermore, their excitation can be described under the quasi-static approximation, in which retardation effects are neglected and a constant phase over the particle is assumed. Using this approximation, the electromagnetic response of the particle takes the form of a static electric dipole with a harmonic time dependence [76]. The dipolar charge distribution (see Figure 5D) induced in the particle by the external electric field, $\mathbf{E}_0$, is described by the electric dipole moment $\mathbf{p} = \alpha\varepsilon_d\mathbf{E}_0$, where α is the electric polarizability of the particle. For the case of a spherical nanoparticle, one obtains [76]

$$\alpha = 3V\frac{\varepsilon_m - \varepsilon_d}{\varepsilon_m + 2\varepsilon_d}, \tag{48}$$

where V is the volume of the nanoparticle. In this case, the LSP resonance occurs at the frequency that satisfies the relation $\varepsilon_m' = -2\varepsilon_d$. Clearly, for the case of a spherical nanoparticle, the resonance frequency only depends on the material properties. This is not the case for other particle shapes. For instance, the electric polarizability of a prolate ellipsoidal nanoparticle is given by [76]

$$\alpha_j = V\frac{\varepsilon_m - \varepsilon_d}{L_j\varepsilon_m + (1 - L_j)\varepsilon_d}, \tag{49}$$

where L_j is a function of the aspect ratio (the ratio of the long axis to the short axis) of the nanoparticle along the axis $j \in \{x, y, z\}$. Hence, its resonance frequency depends on the aspect ratio through L_i. In general, the LSP resonance frequency critically depends on the shape and dimensions of the nanoparticle, enabling a broad tunability across the visible and near-infrared spectrum [77].

At the LSP resonance frequency, a large electric field develops in the nanoparticle due to the large polarizability. Similar to the SPP, the LSP fields peak at the metal surface and decay exponentially away from it. The field enhancement factors exhibited by single nanoparticles, due to this resonant behavior, can vary significantly depending on their shapes. These range from a modest enhancement in gold nanospheres to an enhancement of several orders of magnitude in particles with sharp edges.

LSPs can also exist in subwavelength apertures constructed on thin metallic films. These plasmonic modes are similar to the LSPs supported by nanoparticles in

the sense that their electromagnetic response depend critically on geometrical factors. For example, size and shape of the aperture as well as the thickness of the metal film and the surrounding dielectric. The near fields of LSPs supported by planar particles and apertures can be qualitatively related by Babinet's principle of complementarity [78, 79], which results in electric and magnetic near-fields with complementary distributions for both types of structures. For instance, Figure 5E shows schematically the charge distribution induced by a *y*-polarized electric field, $\mathbf{E}_0$, on a metallic disk and a circular aperture. Dipole moments with opposite directions develop in the nanostructures because the field lines in the metallic region oppose the external field $\mathbf{E}_0$. Figure 5F shows the magnitude of the main electric and magnetic field components, E_y and H_x, of the LSPs supported by a gold disk and a circular aperture with the same diameter (150 nm) and thickness (30 nm). These results clearly show the complementarity of the spatial distribution of electric and magnetic fields [79]. For a more detailed review on the electromagnetic properties of plasmonic nanoholes, the readers are referred to Refs. [80, 81].

3.2 Quantization of surface plasmons

Various methods to quantize surface plasmon fields have been proposed in the past. Elson and Ritchie [82] developed the first quantum theory for SPPs. The first microscopic theory to quantize the matter field and the light field was given by Huttner and Barnett [83], extending the Hopfield approach [84] to include material losses. Also, a macroscopic quantization method was recently proposed by Philbin [85] using Green's functions. Here, we briefly describe two basic quantization methods for SPPs and LSPs [86, 87], which start from the classical macroscopic description of the fields accounting for the dispersive nature of plasmonic material systems. We consider first the case of an SPP mode supported by the metal-dielectric interface illustrated in Figure 5A. Using Coulomb's gauge, the electric and magnetic fields can be obtained from the vector potential, $\mathbf{A}(\mathbf{r}, t)$, which can be cast in the following form:

$$\mathbf{A}(\mathbf{r},t)=\int\frac{d^2\mathbf{K}}{(2\pi)^2}\alpha_{\mathbf{K}}\mathbf{u}_K(z)\exp(i\mathbf{K}\cdot\mathbf{r})\exp(-i\omega t)+\text{c.c.} \tag{50}$$

Here, $\mathbf{K}$ is the SPP wavevector and $\alpha_{\mathbf{K}}$ is the corresponding complex amplitude associated with each of the $\mathbf{K}$ vectors. At this point, we ignore the losses of the system and assume that $\mathbf{K}$ is a real valued quantity. The effect of losses will be incorporated later in this procedure, rendering $\mathbf{K}$ a complex quantity as it is physically required. The vector, $\mathbf{u}_K$, which represents the plasmonic mode, can be written as

$$\mathbf{u}_K=\frac{1}{\sqrt{L(\omega)}}\exp(ik_{zj}z)\left(\hat{\mathbf{K}}-\frac{K}{k_{zj}}\hat{\mathbf{z}}\right), \tag{51}$$

where $L(\omega)$ is a normalization constant with dimensions of length. $\hat{\mathbf{K}}$ and $\hat{\mathbf{z}}$ are unit vectors along the *x* and *z* axes, respectively. Now, consider a square of sides L_x and L_y in the *x*-*y* plane whose area, $S=L_x\times L_y$. This leads to quantized values of wavevector $K_x=n_x2\pi/L_x$ and $K_y=n_y2\pi/L_y$, where n_x, $n_y\in$ Z; now, Eq. (50) can be cast into a summation as

$$\mathbf{A}(\mathbf{r},t)=\sum_{\mathbf{K}}\mathbf{A}_{\mathbf{K}}\mathbf{u}_{\mathbf{K}}(z)\exp(i\mathbf{K}\cdot\mathbf{r})\exp(-i\omega t)+\text{c.c.}. \tag{52}$$

Using this expression and recasting the electric and magnetic fields in the expression for free space energy density [76], $u=1/2(\varepsilon_0\mathbf{E}(\mathbf{r},t)^2+1/\mu_0\mathbf{B}(\mathbf{r},t)^2)$, gives the total energy of the surface wave [86]

$$U=\sum_{\mathbf{K}}\varepsilon_0\omega^2S[A_{\mathbf{k}}A^{\star}_{\mathbf{k}}+A^{\star}_{\mathbf{k}}A_{\mathbf{k}}]. \tag{53}$$

Note that, for each of the modes labeled by $\mathbf{K}$, the energy of the surface wave has the same form as that of the energy of a harmonic oscillator. Hence, by mapping $A_{\mathbf{k}}\rightarrow\sqrt{\frac{\hbar}{2\varepsilon_o\omega S}}\hat{a}_{\mathbf{K}}$ and $A^{\star}_{\mathbf{k}}\rightarrow\sqrt{\frac{\hbar}{2\varepsilon_o\omega S}}\hat{a}^{\dagger}_{\mathbf{K}}$ and using the Hamiltonian of a harmonic oscillator, we obtain the Hamiltonian of the system $\hat{H}=\sum_{\mathbf{K}}\frac{\hbar\omega}{2}[\hat{a}_{\mathbf{K}}\hat{a}^{\dagger}_{\mathbf{K}}+\hat{a}^{\dagger}_{\mathbf{K}}\hat{a}_{\mathbf{K}}]$. As in the formalism of the harmonic oscillator [43], $\hat{a}_{\mathbf{K}}$ is the annihilation and $\hat{a}^{\dagger}_{\mathbf{K}}$ is the creation operators as defined in Eq. 11 and Eq. 12, such that $\hat{a}^{\dagger}_{\mathbf{K}}|n_{\mathbf{k}}\rangle=\sqrt{n_{\mathbf{K}}+1}\,|n_{\mathbf{k}}+1\rangle$ and $\hat{a}_{\mathbf{K}}|n_{\mathbf{k}}\rangle=\sqrt{n_{\mathbf{K}}}\,|n_{\mathbf{k}}-1\rangle$. The fields can now be written as operators acting on the eigenstate $|n_{\mathbf{k}}\rangle$ as

$$\hat{\mathbf{E}}(\mathbf{r},t)=i\sum_{\mathbf{K}}\sqrt{\frac{\hbar}{2\varepsilon_oS}}\mathbf{u}_{\mathbf{K}}(z)\hat{a}_{\mathbf{K}}\exp(i\mathbf{K}\cdot\mathbf{r})\exp(-i\omega t)+\text{H.c} \tag{54}$$

$$\hat{\mathbf{B}}(\mathbf{r},t)=i\sum_{\mathbf{K}}\sqrt{\frac{\hbar}{2\varepsilon_o\omega S}}\mathbf{b}_{\mathbf{K}}(z)\hat{a}_{\mathbf{K}}\exp(i\mathbf{K}\cdot\mathbf{r})\exp(-i\omega t)+\text{H.c}, \tag{55}$$

where $\mathbf{b}_{\mathbf{K}}=(\mathbf{K}+\gamma_i\hat{\mathbf{z}})\times\mathbf{u}_{\mathbf{K}}$ and H.c is the Hermitian conjugate.

The effect of losses due to material dispersion can be incorporated into the formalism by including

interactions of the SPP with a continuum of bath modes [20]. Here, the interaction of the SPP with the bath modes upon propagation modifies the SPP wavevector, **K**, such that it accounts for the complex permittivity of the metal [20].

The quantization of LSPs in metallic nanospheres is carried out by considering a nanoparticle as an optical resonator and by finding its quantized optical modes. The discrete modes are identified as localized solutions of Maxwell's equations [87]. For instance, the electric field distribution associated with the resonant modes of a nanosphere with permittivity ε_m and radius d, at position $\mathbf{r}$ with respect to its center, is given by

$$\mathbf{G}_i = \begin{cases} \hat{\mathbf{i}} & r < d \\ -\frac{d^3}{r^3}(3(\hat{\mathbf{i}}\cdot\hat{\mathbf{r}})\hat{\mathbf{r}} - \hat{\mathbf{i}}) & r > d \end{cases} \tag{56}$$

where $\hat{\mathbf{i}} = \{\hat{\mathbf{x}}, \hat{\mathbf{y}}, \hat{\mathbf{z}}\}$ represents the unit vector along different coordinates. The quantized electric field operator is

$$\hat{\mathbf{E}} = \sum_i \sqrt{\frac{\hbar\omega_0}{2\varepsilon_0 V}} \frac{\mathbf{G}_i}{\sqrt{2(\varepsilon_m + 1)}} (\hat{\mathbf{a}}_i + \hat{\mathbf{a}}_i^\dagger). \tag{57}$$

Here, $\hat{\mathbf{a}}_i$ is the bosonic field operator [87] and

$$V = \frac{4}{3}\pi d^2 \frac{2\varepsilon_m + 1}{\varepsilon_m + 1} \tag{58}$$

is the mode volume, which depends on the dimensions and material properties of the nanosphere. As for the SPP case, the losses of the system can be incorporated in the quantization through the interaction of the fields with a reservoir of bath modes. Other more rigorous approaches based on Green's function formalism have been proposed, enabling the quantization of surface plasmons in more general three-dimensional systems, including the effect of losses, dispersion, and material inhomogeneities [88, 89].

3.3 Quantum effects in plasmonic systems

An important property of plasmonic systems is their capacity to enhance the spontaneous emission rate of quantum emitters, such as molecules or quantum dots. This enhancement, known as the Purcell effect, results from the large density of electromagnetic states existing in the close vicinity of plasmonic structures [90–94]. The Purcell enhancement factor, which is inversely proportional to the mode volume, can be extremely large in plasmonic structures because of their ability to confine the fields to subwavelength dimensions [95–97]. As a result, plasmonic systems have been recognized as important candidates for developing novel single-photon sources with enhanced efficiency [98–100]. Within this context, a recent analysis reported that the theoretical limit for photon-rate enhancement in plasmonic systems can be two orders of magnitude larger than those in their photonic counterparts (i.e. dielectric cavities) [101]. Indeed, these results together with the recent demonstration of room-temperature strong coupling between quantum emitters and LSPs [102] suggest an exciting road ahead for the development of efficient single-photon sources. Although the topic of plasmon-enhanced single-photon emission is quite relevant in quantum plasmonics, a review of this topic is beyond the scope of this work. For more details about this subject, we refer the reader to the following references [23, 95, 103–106].

It has also been demonstrated over the past decades that surface plasmons show exotic quantum properties just like photons. Remarkable examples include wave-particle duality [107], nonlocality [108–114], entanglement [115, 116], tunneling [117–119], bunching and antibunching [120, 121], etc. However, the possibility of preserving quantum mechanical properties in scattering interactions among photons and plasmons has attracted particular attention from multiple research communities in recent years. As described below, this peculiar feature of hybrid photonic-plasmonic systems offers new mechanisms to control fundamental properties of quantum many-body systems [115, 116, 122].

The wave-particle duality is one of the fundamental properties of quantum mechanical systems. In this regard, plasmons have shown self-interference and antibunching effects that demonstrate their undulatory and corpuscular behaviors, respectively [107]. Furthermore, plasmons have also shown wave-particle duality simultaneously [120]. Last but not least, quantum tunneling has been observed in plasmonic systems, for cases in which the separation between nanoparticles is of the order of few angstroms. It has also been shown that tunneling effects can modify the optical response of plasmonic nanogaps in dramatic fashions [21]. There has been an enormous interest in exploring wave-particle duality and quantum tunneling in plasmonic systems. The reader can find additional discussions in the review articles by Zhu et al. [22] and by Xu et al. [23].

4 Quantum statistics in multiparticle photonic-plasmonic systems

4.1 Multiphoton and multiparticle interactions

As illustrated in Figure 6A, multiparticle scattering can be controlled through electromagnetic near-field effects [32, 33, 123–126]. Remarkably, the possibility of manipulating quantum systems at this fundamental level represents one of the most important motivations behind the field of quantum plasmonics and, in general, behind the field of quantum optics [31, 127]. Indeed, the performance of a significant number of quantum protocols depends on the control of complex quantum interactions in systems composed of multiple particles [128–133]. In fact, the future of multiple quantum photonic technologies for information processing depends, to an important extent, on the level of control of quantum effects in multiphoton systems [134]. In this regard, photonic-plasmonic systems provide a flexible platform to investigate quantum multiparticle dynamics. The interest in these hybrid platforms has been triggered by recent progress in the generation of nonclassical multiphoton sources [32, 33, 115, 116, 135–145]. Although, the losses in plasmonic systems and the low photon fluxes that characterize typical quantum sources of light impose challenges to the field of quantum plasmonics. Hitherto, these problems have been partially alleviated using multiple single-photon sources. However, there have been recent breakthroughs in the development of nonclassical single-photon and multiphoton sources. Indeed, the improvement in the generation and engineering of mesoscopic states of light have enabled the investigation of quantum properties of hybrid photonic-plasmonic systems at the mesoscopic scale. For example, in 2016, Harder et al. demonstrated a source for mesoscopic quantum optics with mean photon numbers above 20. This source used SPDC processes in nonlinear waveguides [146]. Later, Magaña-Loaiza et al. demonstrated a tunable multiphoton source that enabled the engineering of quantum statistics and nonclassical correlations of entangled multiphoton states [147].

The large variety of scattering events that can take place in many-body systems of photons offers new paths to perform quantum information processing. Interestingly, the complexity and control of underlying scattering events can be boosted through the enhancement of electromagnetic near-fields by means of surface plasmons. In general, surface plasmons offer the possibility of achieving novel light-matter interactions [127]. Below, we review recent research achievements along this research line.

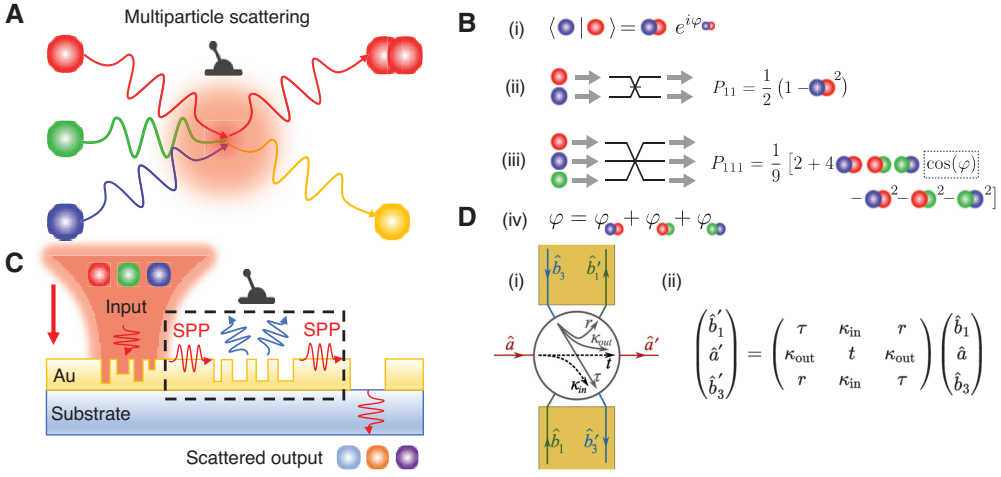

Figure 6: Multiparticle scattering in hybrid photonic-plasmonic systems.
(A) Concept behind the control of multiphoton dynamics through the manipulation of electromagnetic near-fields. Interestingly, multiphoton interference in multiport devices can be used to investigate fundamental physics behind multiparticle scattering. (B) Summary of the importance of indistinguishability and the overall phase φ for two- and three-photon interactions. (i) Concept of indistinguishability for two photons. (ii) A simplified version of the HOM experiment. (iii and iv) Process of three-photon interference and the idea behind the collective phase φ, respectively. Reproduced from Ref. [123]. (C) Remarkably, these effects can be manipulated in plasmonic nanostructures through the engineering of metallic gratings and slits. This hybrid quantum device enables the possibility of engineering multiparticle scattering and consequently multiparticle interference. (D) Photon-plasmon scattering has been demonstrated in hybrid photonic-plasmonic tritters [(i) and (ii)]. The plasmonic tritter couples a photonic mode $\hat{a}$ to two plasmonic modes $\hat{b}_1$ and $\hat{b}_3$. Reproduced from Ref. [33].

However, for the sake of clarity, we first describe underlying ideas behind multiparticle interactions.

In Section 2.4, we revisited the HOM experiment, where two photons injected into the input ports of a 50/50 beam splitter interfere and exhibit photon bunching. As illustrated in Figure 6B (i), the distinguishability of two photons in states $|\phi_i\rangle$ and $|\phi_j\rangle$ can be quantified through the inner scalar product of the two states as $\langle\phi_i|\phi_j\rangle = r_{ij}e^{i\varphi_{ij}}$. Here, the modulus of r_{ij} can be interpreted as a measure of distinguishability between the two photons. The probability of detecting one photon in each of the output ports of a beam splitter only depends on the degree of distinguishability as $P_{11} = \frac{1}{2}(1-r_{ij}^2)$. In general, the argument $e^{i\varphi_{ij}}$ does not play a relevant role in two-photon interference. Surprisingly, quantum interactions in systems with more than two photons cannot be exclusively described by the degree of indistinguishability between pairs of photons [125, 148, 149]. In 2017, Menssen et al. demonstrated that particle indistinguishability is not enough to describe multiphoton interactions involving more than two photons [123]. In this work, the team unveiled the complexity behind multiphoton interference in a quantum mechanical tritter, a multiport device with three inputs and three equally likely outputs. As shown in Figure 6B (iii), three-photon interference shows a strong dependence on the collective triad phase defined as $\varphi = \varphi_{12} + \varphi_{23} + \varphi_{31}$ [Figure 6B (iv)]. Generally, three-photon interference can be described as

$$P_{111} = \frac{1}{9}[2 + 4r_{12}r_{23}r_{31}\cos(\varphi) - r_{12}^2 - r_{23}^2 - r_{31}^2]. \quad (59)$$

These quantum interactions in photonic systems can be controlled through plasmonic effects. As illustrated in Figure 6C, the series of scattering events induced by photon-plasmon-photon conversions can be used to control global phases and thus multiphoton interference in quantum many-body systems. These ideas have been discussed in the context of plasmonic multiport devices in metallic slits (see Figure 6D). As discussed below, these mechanisms also offer the possibility to preserve and manipulate multiphoton coherence [121, 127, 150–154]. Later in this review, we will describe recent demonstrations of quantum control in hybrid photonic-plasmonic systems.

4.2 Quantum statistics of photonic-plasmonic systems

As previously discussed, plasmonic effects can be used to control the quantum interactions in quantum systems. Despite the inherent losses that characterize quantum plasmonic systems, properties in photon-plasmon scattering processes offer new mechanisms to exert control of multiparticle systems [115, 116, 136, 141]. For example, in 2009, Huck et al. demonstrated that quadrature squeezing was preserved in the photon-plasmon-photon process even in the presence of linear loss and decoherence [137]. In their experimental setup (Figure 7A), squeezed light was generated in an optical parametric oscillator and then coupled to a gold stripe. Then, the scattered photons from the plasmonic setup were collected and analyzed to certify squeezing. In Figure 7B, one can observe that, although quadrature squeezing is degraded, the squeezing was coherently transferred through the photon-plasmon-photon process. It was further confirmed that plasmonic interactions can be described by an unitary beam splitter transformation [20, 137].

More recently, Martino et al. characterized the role that losses play in the quantum statistics of the electromagnetic field in plasmonic waveguides [138]. In their setup (Figure 7C), a type I SPDC source was used to generate entangled photon pairs. The team used one of the generated modes to excite an SPP mode in the thin metallic stripe waveguide. By measuring the photon number distribution of multiple output states and the second-order quantum coherence functions $g^{(2)}(\tau)$ (Figure 7D), it was demonstrated that losses in quantum plasmonic systems behave similarly to that predicted by the classical theory of uncorrelated Markovian linear loss. Furthermore, due to the fact that photon-plasmon-photon processes do not modify the second-order coherence function $g^{(2)}(\tau)$, it is possible to fabricate larger SPP waveguide structures for quantum control.

Undoubtedly, the phase associated to quantum states plays a fundamental role in multiple applications [156]. In the context of quantum control, the manipulation of sequential photon-plasmon scattering processes in plasmonic gratings has enabled the control of geometric phases in single-plasmon systems. The phase of quantum systems plays an important role in quantum interactions, particularly in interference effects [123]. In this regard, Daniel et al. showed that photon-plasmon-photon processes preserve the well-known Pancharatnam-Berry geometric phase [155]. This study was carried out through a Mach-Zehnder interferometer (Figure 7E). The averaged and fitted data for different polarization states are shown in Figure 7F. These figures illustrate that the shifts of the peaks are proportional to the change in polarization, which is an indication of the conservation geometric phase in photon-plasmon-photon processes.

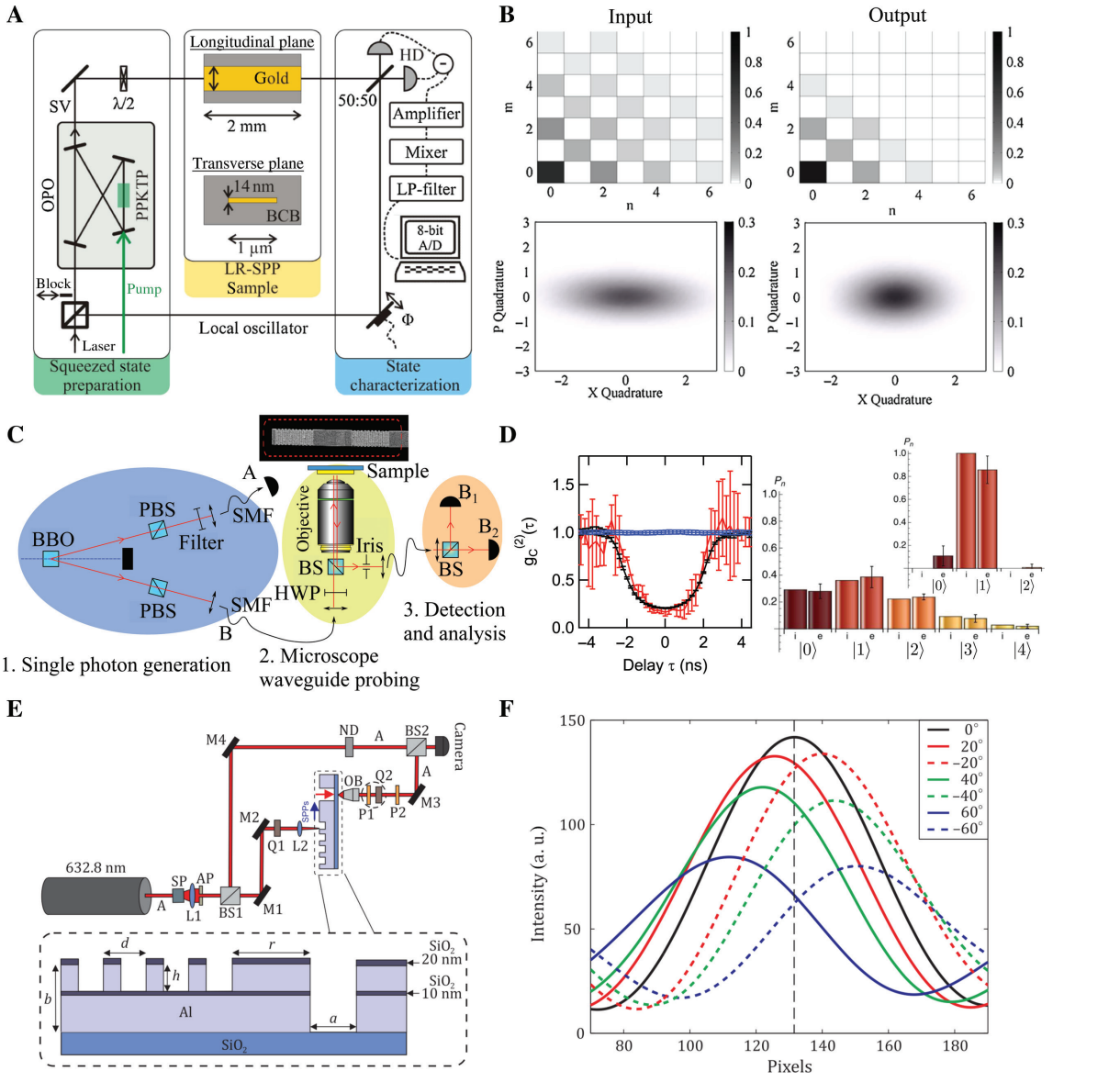

Figure 7: Experiments that demonstrate the preservation of quantum statistics in hybrid photonic-plasmonic systems. (A) Schematic of the experimental setup used for demonstration of quadrature squeezing preservation. OPO, optical parametric oscillator; PPKTP, periodically poled potassium titanyl phosphate crystal; SV, squeezed vacuum. (v) Experimentally generated and transmitted squeezed vacuum states after a photon-plasmon-photon process. The quadrature of the electric field, absolute values of the reconstructed density matrices, Wigner functions, and noise power relative to the shot noise level of input and output are also presented. (A and B) Reproduced from Ref. [137]. (C) Schematic of the setup used for the experimental demonstration of the preservation of quantum statistics in plasmonic waveguides. (D) Conditional second-order quantum coherence functions $g^{(2)}(\tau)$ for light with nonclassical and classical statistical properties. The dotted blue line illustrates the classical limit. Right, corresponding two-photon number distributions. (c and d) Reproduced from Ref. [138]. (E) Schematic of the experimental setup for plasmonic control of the Pancharatnam-Berry geometric phase. This is demonstrated through the interference patterns in (F). The shift of interference fringes unveils the possibility of preserving geometric phases in plasmonic systems. AP, aperture; BS, 50/50 beam splitter; L, lens; M, mirror; ND, neutral density filter; OB, microscope objective; P, linear polarizer; SP, spatial filter; Q, quarter-wave plate. (e and f) Reproduced from Ref. [155].

4.3 Preservation of entanglement in plasmonic systems

Entanglement is one of the most remarkable consequences of quantum physics [68]. In addition, it constitutes a critical resource for multiple applications, including quantum imaging [66, 157–160], quantum key distribution [161–165], quantum computation [166–168], and quantum communication [169, 170]. Given the potential of entanglement for the development of quantum technologies, it is always

desirable to investigate paths to preserve it in complex processes involving light-matter interactions. The possibility of preserving quantum entanglement in photon-plasmon-photon interactions makes quantum plasmonic systems a promising platform for quantum technologies [23, 171, 172]. In this regard, Altewischer et al. [115] initiated the field of quantum plasmonics with their experimental verification of the preservation of polarization entanglement in plasmonic systems. This seminal work demonstrated the possibility of preserving polarization entanglement in photon-plasmon-photon conversion processes. As shown in Figure 8A, correlated photon pairs generated through SPDC were transmitted through an array of holes in a gold film where the photon-plasmon-photon conversion takes place. The team certified entanglement between two detected light beams. This experiment demonstrated the possibility of generating entanglement between plasmonic and photonic modes. Although entanglement is preserved, the team also showed that, when focusing one of the beams onto a single hole in the metallic structure, the degree of entanglement decreased. This was observed through a reduction in the visibility associated to biphoton interference.

This work stimulated new fundamental research. For example, Moreno et al. [173] reported a quantum description of the underlying physics behind plasmon-assisted transmission. They theoretically showed that the degradation of entanglement arose from the polarization sensitivity of gold gratings. Furthermore, the scattering theory of plasmon-assisted entanglement transfer and distillation was introduced by van Velsen et al. [174]. Since then, the preservation of entanglement has been further explored by different groups under multiple experimental conditions [136, 140, 175]. Fakonas et al. showed path entanglement between surface plasmons [176]. Ren et al. further demonstrated that entanglement based on orbital angular

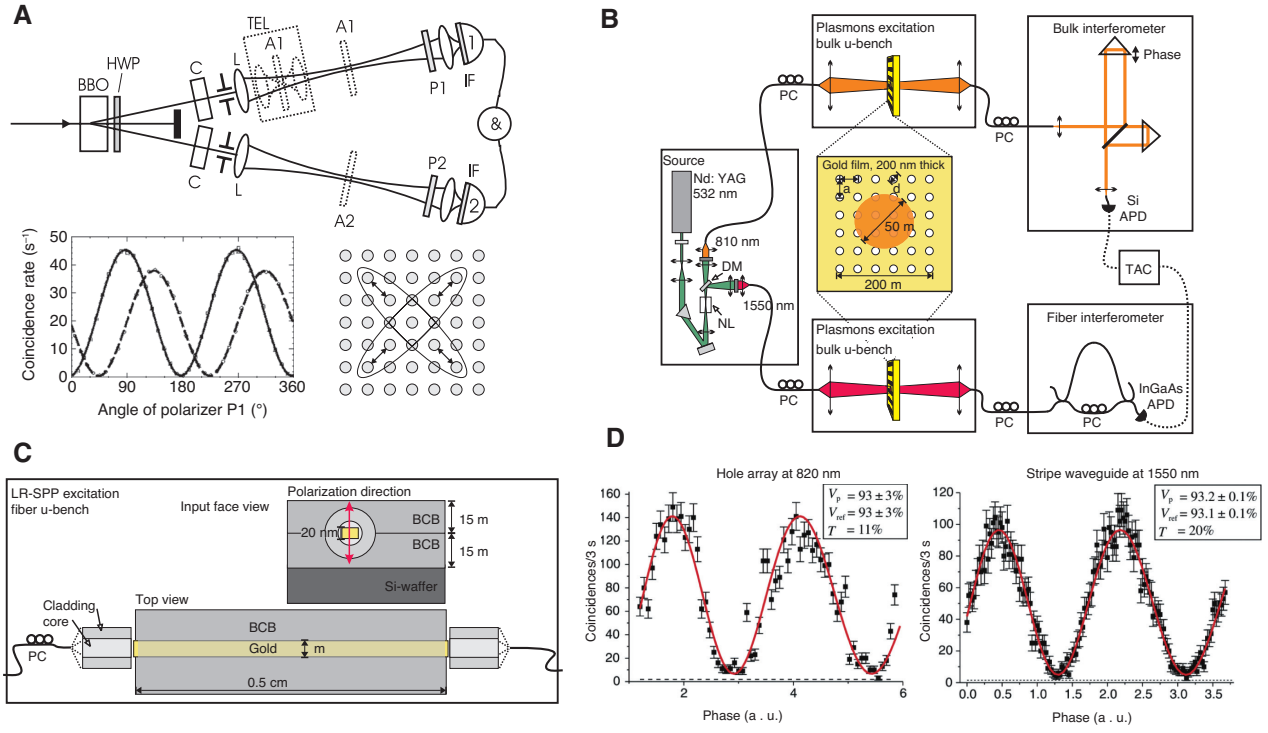

Figure 8: Experiments demonstrating entanglement preservation in plasmonic systems.
(A) First experiment that demonstrated plasmon-assisted transmission of entangled photons. This was confirmed through the measurement of two-photon quantum interference after photon-plasmon-photon conversion, which demonstrated the preservation of entanglement. The experimental setup used a β barium borate (BBO) nonlinear crystal to generate entangled photon pairs that were passed through an array of gold. The generated light beams were detected by two single-photon detectors. C, compensating crystals; HWP, half-wave plate; IF, interference filters; L, lens; P1 and P2, polarizers; TEL, confocal telescope. Reproduced from Ref. [115]. (B) Schematic of the experimental setup demonstrating energy-time entanglement in a plasmonic system. APD, avalanche photodiode; DM, dichroic mirror; NL, nonlinear crystal; PC, polarization controller; TAC, time to analogue converter. (C) Schematic of the LR-SP waveguide. BCB, benzocyclobutene. (D) Experimental interference fringes produced by the setups shown in (B) and (C). V_p represents the visibility of the interference fringes after plasmonic conversion. Furthermore, V_{net} describes the visibility in the absence of plasmonic conversion, and T is the transmittance of the plasmonic setup. (B–D) Reproduced from Ref. [116].

momentum is preserved in photon-plasmon-photon processes [139]. Last but not least, Asano et al. showed that plasmonic metamaterials can be used for entanglement distillation [177].

Particularly, in 2005, Fasel et al. showed that energy-time entanglement was also persevered in photon-plasmon-photon scattering processes [116]. In their experiment, the preservation of energy-time entanglement was demonstrated using subwavelength metallic hole arrays and long-range surface plasmons (LR-SP) propagating in metallic waveguides. Their setup shown in Figure 8B used two different wavelengths of 810 and 1550 nm. The metallic hole arrays were carefully designed to maximize photon-plasmon-photon conversion. In addition, the setup for LR-SP waveguide shown in Figure 8C was used to confirm photon-plasmon-photon scattering. This arrangement enabled the induction of time delays that are essential to test energy-time entanglement. The interference visibility shown in Figure 8D demonstrated preservation of energy-time entanglement in photon-plasmon-photon processes.

The experiments described above exploited quantum interactions among photons in plasmonic structures with overall sizes larger than their wavelengths λ. More recently, smaller metallic structures with sizes comparable to λ have been used to perform quantum plasmonics. Li et al. experimentally demonstrated that polarization entanglement can be maintained in these metallic structures [178]. Their setup shown in Figure 9A used a type I SPDC source and a nanoscale hybrid plasmonic waveguide to preserve quantum polarization entanglement. The generated polarization entangled two-photon Bell state $|\Phi^+\rangle = 1/\sqrt{2}(|HH\rangle + |VV\rangle)$ was tuned to achieve an output fidelity of 0.932 after the photon-plasmon-photon conversion. Additionally, the team verified entanglement by performing a series of projective measurements. This was confirmed by the measured fourth-order quantum interference structure shown in Figure 9B. This work was further explored through a demonstration of the propagation of polarization entangled two-photon N00N states in a nanowire [179]. In their work, Chen et al. generated the polarization entangled N00N state $|\mathrm{N00N}\rangle = 1/\sqrt{2}(|2_H, 0_V\rangle - |0_H, 2_V\rangle)$, which was coupled into a nanowire. The team verified the preservation of the N00N state using two-photon HOM interference shown in Figure 9C. The team was able to observe visibilities of 0.737 ± 0.007 and 0.880 ± 0.013 for single- and two-photon N00N state input, respectively. In Figure 9D, it is possible to identify the doubled oscillation period produced by particles prepared in a N00N state, where $N = 2$.

Furthermore, Büse et al. demonstrated symmetry protection of quantum entanglement through the interaction with a single nanoaperture [180]. As shown in Figure 9E, the group of scientists used Bell states that were strongly focused on a metallic nanoaperture to demonstrate the potential of dissipative near-fields to preserve quantum coherence.

Indeed, the protection of two-photon entangled states based on polarization exploited the polarization sensitivity of a metallic nanoaperture. Interestingly, this simple system acts as a lossy beam splitter that endowed this protocol with a unique sensitivity to the relative quantum phase between the entangled modes [127, 181, 182]. The experimental results that demonstrate symmetry protection are presented in Figure 9F. The quantum tomography of the transmitted state suggests that the state $|\Psi_-\rangle$ is unaffected, whereas the state $|\Psi_+\rangle$ is mixed with $|\Psi_0\rangle$, where

$$\begin{aligned} |\Psi_+\rangle &\to \frac{1}{\sqrt{2}}(|R\rangle_1|R\rangle_2 + |L\rangle_1|L\rangle_2), \\ |\Psi_-\rangle &\to \frac{1}{\sqrt{2}}(|R\rangle_1|R\rangle_2 - |L\rangle_1|L\rangle_2), \\ |\Psi_0\rangle &\to \frac{1}{\sqrt{2}}(|R\rangle_1|L\rangle_2 + |L\rangle_1|R\rangle_2), \end{aligned} \tag{60}$$

and $\hat{a}^\dagger_{0,+/-}|0\rangle \to |R/L\rangle$.

5 Quantum interactions in quantum plasmonics

5.1 Multiparticle quantum interference in photonic-plasmonic systems

Quantum interference has been extensively used as a tool to manipulate quantum mechanical systems [183]. Interestingly, the conditions under which multiparticle interference occurs can be controlled through photon-plasmon scattering. In 2013, Heeres et al. demonstrated the first quantum interference experiment in a plasmonic platform [151]. As shown in Figure 10A, the team used a free-space source of SPDC, a plasmonic directional coupler as beam splitter, and on-chip detectors to perform HOM interference. The ideal HOM dip visibility for their SPDC source is estimated to be $V = 0.92 \pm 0.01$. The excited single plasmons interfere on the chip leading to HOM dips with visibilities of the order of $V = 0.43 \pm 0.02$ and $V = 0.39 \pm 0.01$ for two different plasmonic devices.

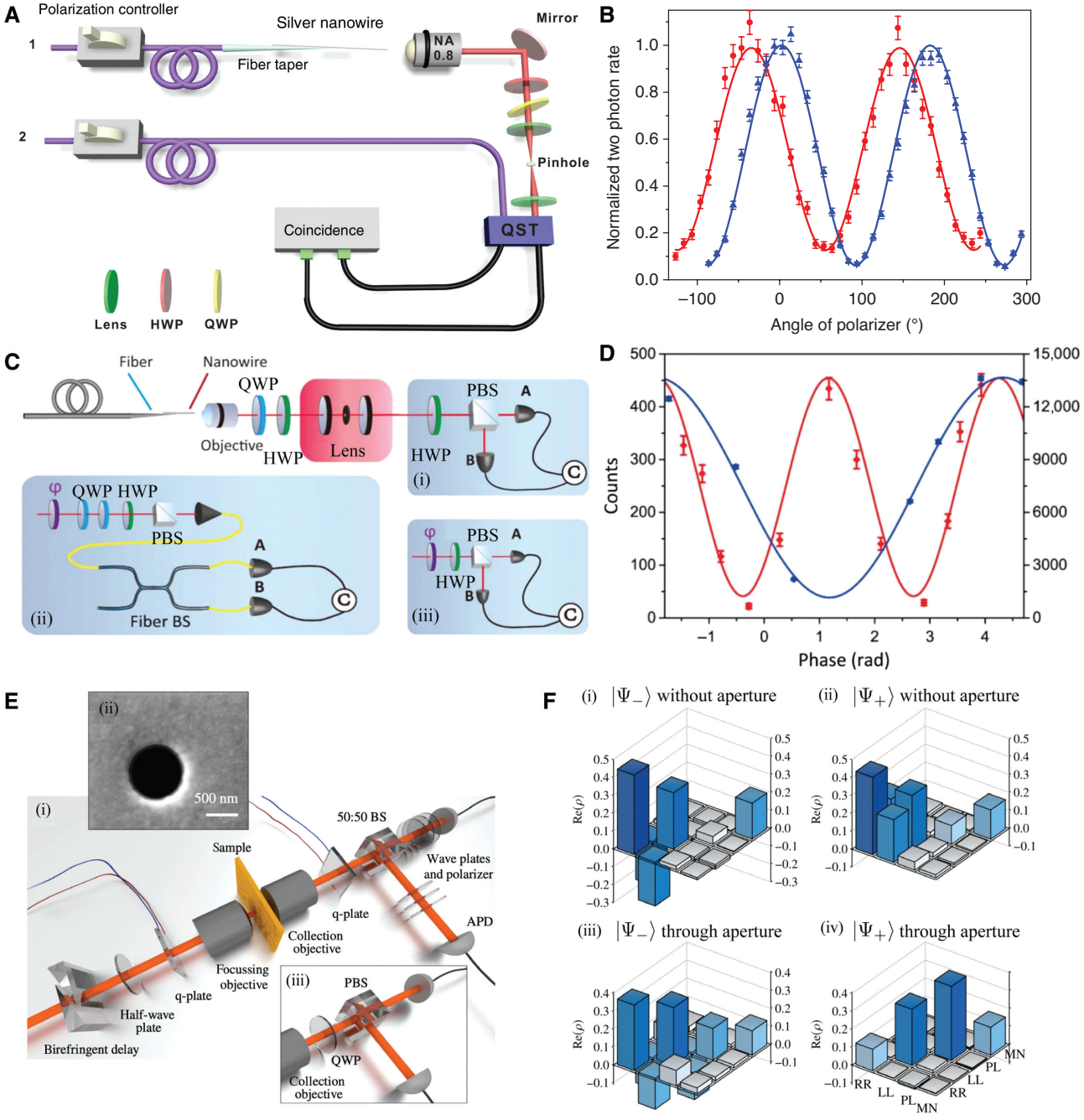

Figure 9: Experiments that demonstrate the preservation of entanglement in plasmonic systems.
(A) Experimental setup used for polarization entanglement in a nanoscale hybrid plasmonic waveguide. In this case, one of the correlated photon pairs is sent to a silver nanowire, whereas the other photon partner is sent to a module for structures state tomography (QST). (B) Quantum interference structures observed through correlation measurements demonstrate the preservation of entanglement. Blue and red dots represent coincidence rates for photons projected onto different polarization states. (A and B) Reproduced from Ref. [178]. (C) Experimental setup for the demonstration of quantum plasmonic N00N states in a silver nanowire. The generated N00N state is transmitted and preserved in the nanowire. The transmitted photons are then forced to interfere in an HOM setup (ii). The arrangement used to measure the de Broglie wavelength of biphotons (iii). The transmitted two-photon entangled state is characterized by quantum state tomography (ii). (D) Two-photon coincidence counts and single-photon counts of the plasmonic N00N state transmitted in (C). The red curve represents the two-photon coincidence, whereas the blue curve represents single-photon counts. (C and D) Reproduced from Ref. [179]. (E) Schematic of the experimental setup for the symmetry protection of entanglement in a single nanoaperture. (F) Quantum tomography of the state $|\Psi_+\rangle$ and $|\Psi_-\rangle$ with and without the nanoaperture interaction. (E and F) Reproduced from Ref. [180].

Typically, the asymmetric losses in photonic-plasmonic systems will decrease the second-order quantum interference visibility. However, careful symmetric designs of plasmonic nanostructures enables one to preserve indistinguishability that leads to high visibilities. As discussed in Section 2.4, the visibility is determined by the degree of indistinguishability between two photons. In this case, reduced visibility was attributed to the excitation of long-range plasmon modes, which are loosely confined plasmonic modes [184].

Despite the fundamental relevance of this experiment, the nonclassical nature of the interference patterns remains unclear. This is due to the fact that the measured interference patterns did not exceed a visibility of 50%. Nevertheless, this pioneering experiment motivated the development of hybrid quantum networks on chip [185, 186]. Later in 2014, Fakonas et al. used a dielectric-loaded SPP waveguide (DLSPPW; Figure 10C) to achieve an HOM visibility of 0.932 ± 0.01 [152]. In addition, Martino et al. also certified the nonclassical nature of interference effects in plasmonic systems [121]. Similar to Ref. [151], Martino et al. used an X-shaped plasmonic beam splitter to demonstrate an HOM visibility of $V = 0.72 \pm 0.13$ (see Figure 10D). These works were followed by multiple experiments that aimed to validate quantum interference in a large variety of plasmonic platforms. For example, Cai et al. observed a visibility of 0.957 ± 0.089 in a similar DLSPPW platform (Figure 10E) [153]. Recently, Fujii et al. observed a visibility of 0.843 ± 0.091 in long-range SPP (LRSPP) waveguides (Figure 10F) [154]. These beautiful experiments indicate that, although surface plasmons are formed from photons (bosons) and electrons (fermions), they indeed exhibit bosonic behaviors in the limit of many-electron regimes. Moreover, quantum plasmonic systems have shown potential for quantum metrology, this due to the importance of quantum interference for metrology. In fact, quantum plasmonic technologies offer a solid platform to implement quantum metrology on chip. Interestingly, the additional quantum interference paths, provided by photon-plasmon scattering processes, have been used to demonstrate coalescence and anticoalescence of a pair of bosons. In 2016, Dheur et al. experimentally verified the wave-particle duality for a single surface plasmon [150]. This experiment made use of asymmetric 11-groove gratings as those illustrated in Figure 10G. By measuring the intensity correlation function of heralded SPPs, they observed single SPPs antibunching in the single-photon-level regime, showing the particle-like nature of SPPs. Moreover, they observed single SPP interference, which certified the wave-like properties of the SPP. This experimental work also revealed fundamental similarities between plasmons and photons.

5.2 Controlling quantum multiparticle interactions

As previously discussed, the control of quantum interference in plasmonic systems has been improved through the use of multiple degrees of freedom of photons and SPPs. Although surface plasmons are well known to suffer from losses, the underlying scattering processes among photons and plasmons provide additional quantum interference paths that are of fundamental importance for controlling decoherence of quantum systems.

Until recently, researchers started to exploit the design of nanostructures as well as their inherent losses to control scattering processes [30, 172, 187–189]. Inspired by their previous research [150], Vest et al. recently modified the reflection and transmission coefficients of a surface plasmonic beam splitter (SPBS) to demonstrate coalescence and anticoalescence of single SPPs [127]. As shown in Figure 11A, the change in the width w, metal gap g, and groove depth h led to different reflection and transmission factors r and t. Furthermore, the parameters r and t provide a unique control of the phase difference between the reflected and transmitted plasmons. Remarkably, the phase in the system leads to exotic interactions that were measured through the implementation coincidence measurements $P(1, 1)$. Indeed, the coincidence detection probability can be modeled as

$$P(1,\ 1) = |t|^4 + |r|^4 + 2\Re(t^2 r^2) I. \tag{61}$$

where $2\Re(t^2 r^2) = t^2 r^{\star 2} + t^{\star 2} r^2$, and I is the overlap between two particles' wave packets, similar to the modulus of r_{ij} described in Figure 6B (i). When two particles' wave packets overlap ($I = 1$), and when the SPBS is 50/50 ($t = \pm ir$ and $t = 1/\sqrt{2}$), the coincidence $P(1, 1) = 0$.

In this case, the completely vanished coincidence resembles the HOM interference effect discussed in Section 2.4, where two single photons coalesce on a lossless beam splitter. Additionally, when the two particles' wave packets are independent ($I = 0$), the coincidence probability resembles the classical case, where

$$P_{\mathrm{cl}}(1,\ 1) = |t|^4 + |r|^4 . \tag{62}$$

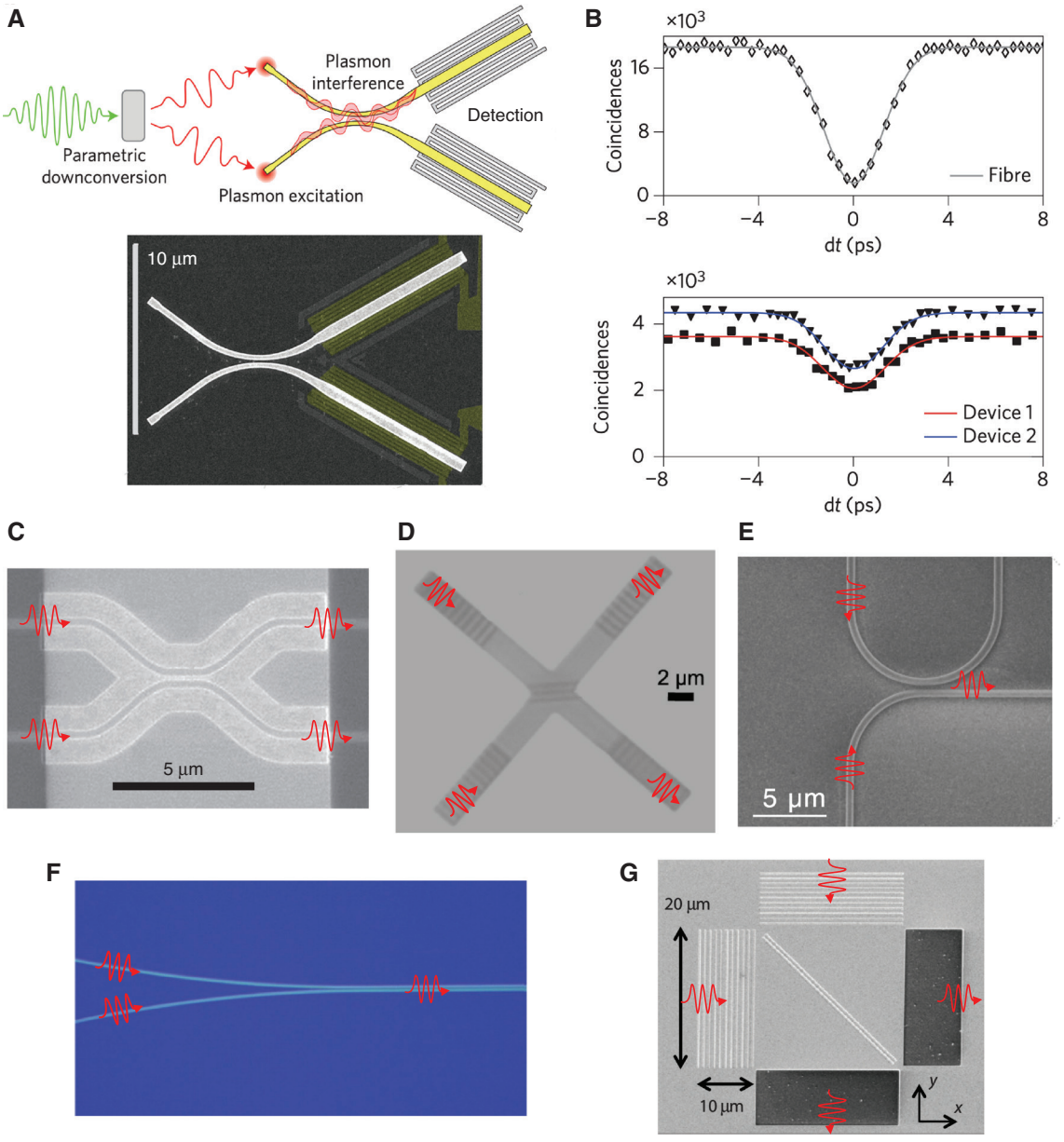

Figure 10: HOM interference with different plasmonic structures for beam splitters.
(A) On-chip HOM interference with single plasmons. The team used photon pairs generated through SPDC to excite single plasmons that were forced to interfere in a plasmonic directional coupler. The scanning electron microscope (SEM) image of the gold plasmonic directional coupler device is also shown. (B) HOM interference dip of the photon pair source and quantum interference traces of single plasmons in two devices. (A and B) Reproduced from Ref. [151]. (C) DLSPPWs patterned by polymethyl methacrylate (PMMA) used in Ref. [152]. Reproduced from Ref. [152]. (D) Optical image of the plasmonic beam splitter used in Ref. [121]. The coupling and decoupling gratings of the plasmonic beam splitter consist of 11 ridges. Reproduced from Ref. [121]. (E) SEM image of part of a typical plasmonic DC structure used in Ref. [153]. Reproduced from Ref. [153]. Reproduced from Ref. [154]. (F) Microscope image of the fabricated LRSPP device used in Ref. [154]. (G) SEM top view of the photon-to-SPP launcher used in Ref. [150]. Reproduced from Ref. [150].

For the case in which $|t| = |r| = 1/2$ and $t = \pm r$, the coincidence probability $P(1, 1) = 2P_{cl}(1, 1)$. This suggests that, instead of getting a dip in the coincidence probability, one would instead get a peak, which indicates the anticoalescence of SPPs. As shown in Figure 11B, two samples of SPBS exhibit coalescence and anticoalescence of SPPs. Particularly, this experiment demonstrated that, although the surface plasmons are typically treated as bosons, they can exhibit fermionic properties.

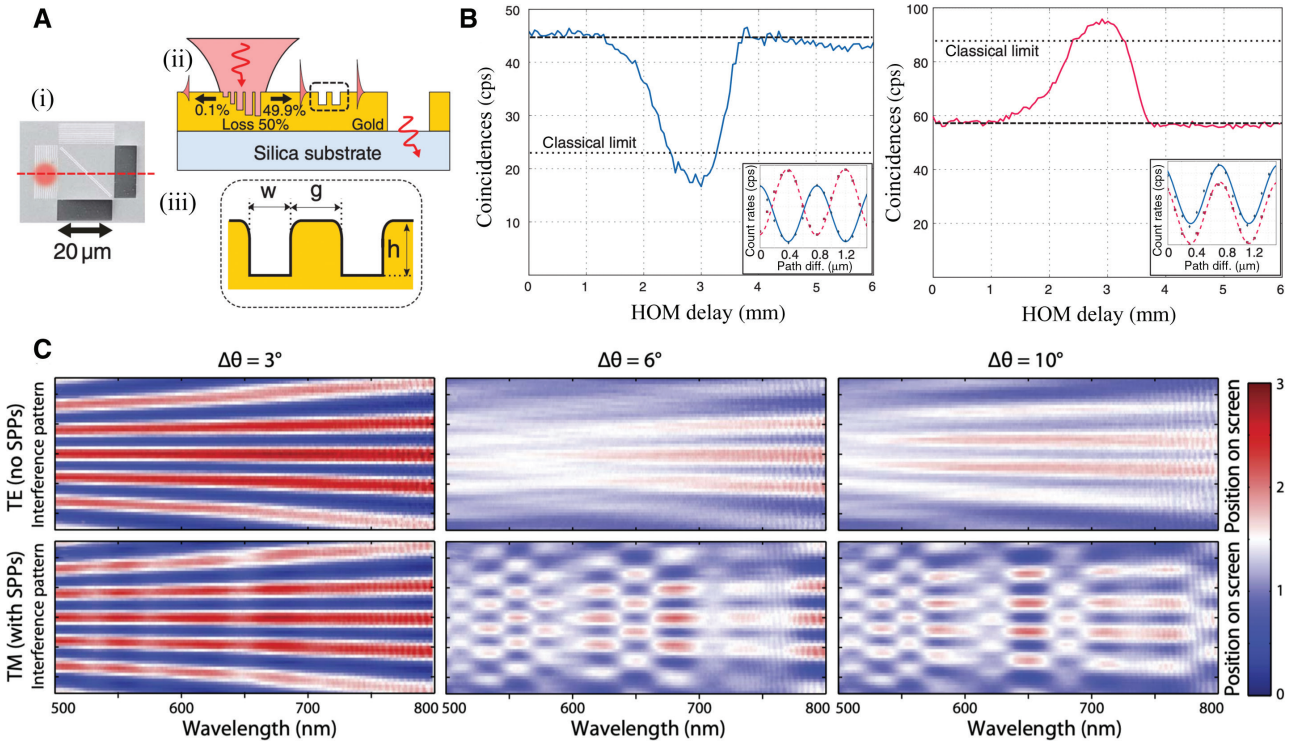

Figure 11: Control of quantum multiparticle interactions.
(A) (i) SEM image of an integrated plasmonic beam splitter. (ii) Cross-section diagram of the integrated plasmonic beam splitter showing the photon-plasmon-photon process. The photons are converted to plasmon on the left, then launched into the plasmonic beam splitter (enclosed by black dashed line), and converted back into photons in the silica substrate. (iii, inset) Grating parameters that are used to control the transmission and reflection of photons in the plasmonic beam splitter. (B) Experimental observation of the plasmonic HOM coalescence/anticoalescence effects. (A and B) Reproduced from Ref. [127]. (C) Control of spatial coherence through surface plasmons in a metallic slit. Reproduced from Ref. [31].

Additionally, single plasmons can also modulate spatial coherence of optical fields [190–195]. Using this feature, Li and Pacifici recently achieved continuous modulation of the degree of spatial coherence with amplitudes ranging from 0 to 80% [31]. By varying the slit's separation, wavelength, and polarization of the incident light beam, they demonstrated the possibility of transforming incoherent optical fields to partially coherent fields and vice versa. As shown in Figure 11C, surface plasmons are generated in a metallic double-slit structure when this is illuminated by light polarized along the incidence plane. These near fields induce a change in the interference pattern formed in the far field of the double slit. These interesting effects demonstrated that, despite the losses in metallic nanostructures, plasmons can be used to enhance spatial coherence of optical fields. Interestingly, the gratings in plasmonics systems can induce phase shifts that can be used to control quantum interactions. Undoubtedly, this possibility enables the control quantum many-body systems of photons.

6 Quantum plasmonic devices and networks for multiparticle systems

The experimental realization of multiphoton quantum protocols relies on the fundamental tenants of quantum mechanics. Interestingly, there have been recent breakthroughs in physics that have unveiled the existence of novel quantum processes [32, 196]. Naturally, these new interactions have extended our understanding of fundamental principles of quantum mechanics such as superposition and particle indistinguishability. For example, Born's rule bounds the complexity of any effect involving superpositions of an arbitrary number of wavefunctions to a sum of ters denoting the interference between pairs of wavefunctions. Thus, in accordance with Born's rule, the interference pattern obtained in a three-slit experiment can be described by the following probabilities

$$P_{ABC} = P_{AB} + P_{BC} + P_{AC} - P_A - P_B - P_C, \tag{63}$$

where the slits are denoted by letters A to C. Note that Eq. (63) does not include a probability term that involves three slits but is entirely described by probabilities involving only one and two slits. Surprisingly, it was recently predicted that a particle in a three-slit experiment has a finite probability of traveling forward through one slit, then loop around and travel back through another slit, and then loop around again and travel forward through a third slit [32]. In general, the probability of observing a photon following a trajectory such as the one depicted in Figure 12A is extremely small. Such an exotic trajectory would require the occurrence of unlikely scattering events in the vicinity of the slits. Interestingly, these exotic interactions could lead to an apparent violation of Born's rule and consequently of the superposition principle.

In 2016, Magaña-Loaiza et al. observed looped trajectories of photons for the first time. The team found out that looped trajectories exist due to near-field effects and that these can be amplified through the excitation of SPPs in metallic slits. In addition, they confirmed the validity of the superposition principle. More specifically, it was demonstrated that strong confinement of the electromagnetic field in the vicinity of the slits produces a dramatic increase in the probability of occurrence of looped

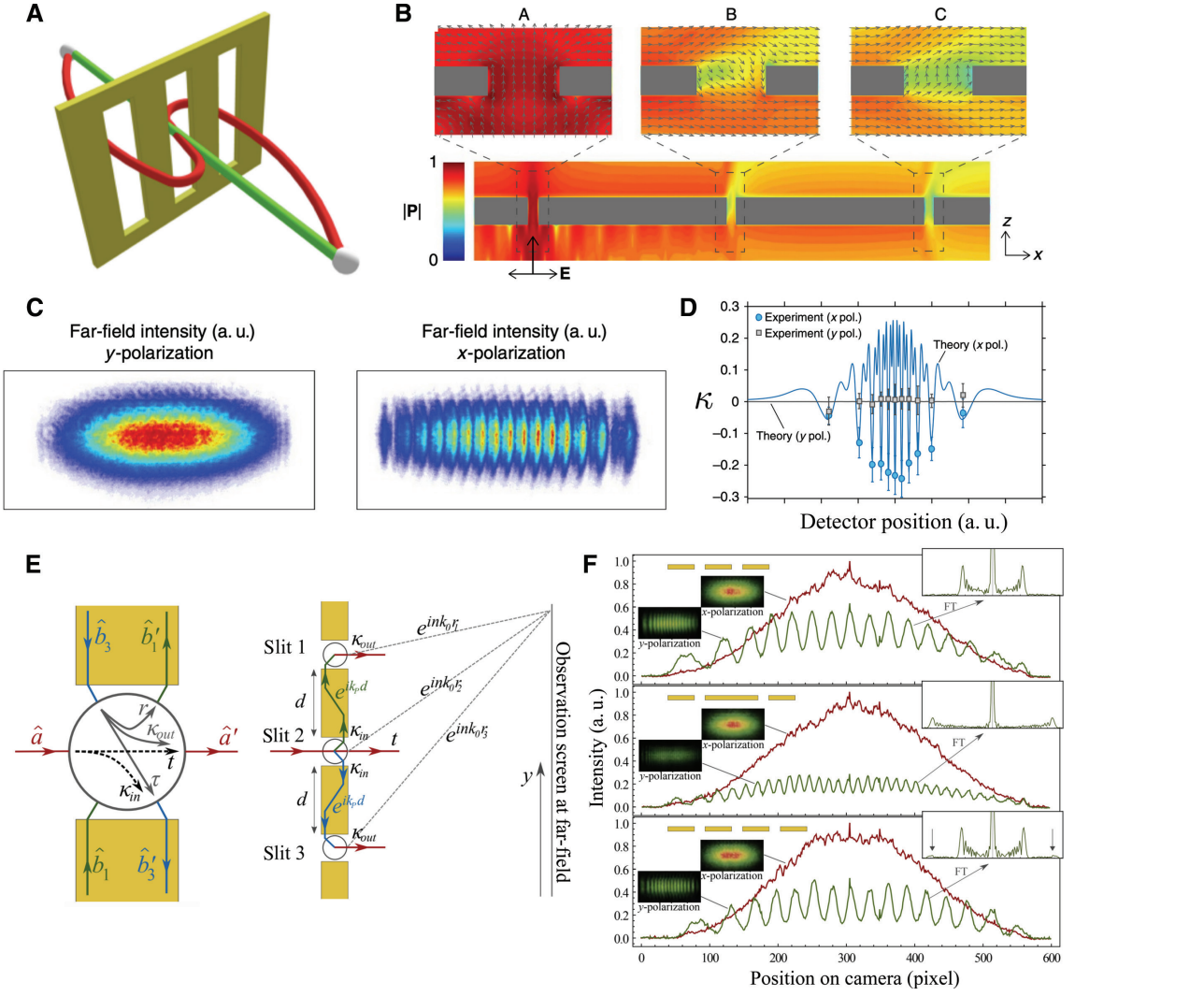

Figure 12: Hybrid photonic-plasmonic multiport devices.
(A) Looped and straight trajectories of photons in a three-slit interferometer. (B) Magnitude of the Poynting vector *P* in the vicinity of metallic slits for a case in which a single slit is illuminated with photons polarized along the *x*-direction. (C) Measured far-field distributions of single photons for the case studied in (B). The appearance of fringes is attributed to interference among photons traveling in straight and looped trajectories. (D) Parameter κ, which quantifies the complexity of the process. (A–D) Reproduced from Ref. [32]. (E) Photon-plasmon scattering processes in a plasmonic tritter and the schematic diagram of the triple-slit structure when each slit is a tritter. (F) Far-field interference patterns from the three different slit structures. Only the photons with *y* polarization excite SPPs (green), whereas no interference occurs for *x* polarization (red). (E and F) Reproduced from Ref. [33].

trajectories. In general, these fields exist in the vicinity of any structure. However, their contribution to other physical processes is always negligible, thus rendering exotic effect such as looped trajectories. Furthermore, Magaña-Loaiza et al. discovered that such exotic dynamics lead to more complicated interference processes that require sophisticated applications of the superposition principle.

In the experiment, they used the polarization of single photons to control the strength of near-fields in the vicinity of slits, in a gold film, through the excitation of surface plasmons. As shown in Figure 12B, the exact solution of Maxwell equations predicts curvy trajectories for the Poynting vector when one of the slits is illuminated by photons polarized along the x-direction but not for those polarized in the y-direction. This due to the strong electromagnetic near-fields confined in the former case. In fact, the geometry of the slits allows for the design of specific looped trajectories. Interestingly, this near-field coupling produces fringes in the far-field. As shown in Figure 12C, this effect enables the use of near-fields to induce or destroy spatial coherence. This is an example in which dissipative near-field dynamics are exploited to improve coherence. The contributions from looped trajectories were quantified through the parameter κ, and this parameter is expected to be zero for a situation in which near-fields are negligible and different from zero if the contributions from near-fields are significant, see Figure 12D.

In addition, the complex photon dynamics observed in the three-slit structure described above shows enormous potential to control interference in quantum networks. It was recently demonstrated by Safari et al. that a quantum mechanical tritter can be implemented through a single plasmonic slit [33]. In addition, they developed a technique to characterize quantum processes in plasmonic networks. Remarkably, the robustness of this technique enabled the first measurement of the phase shift acquired by single photons participating in photon-plasmon scattering processes. In contrast to Feynman's path integral formalism, this technique enables the practical design and characterization of complex plasmonic networks for multiparticle applications in quantum information science.

7 Conclusions

The rapid development of quantum plasmonics has enabled new platforms to prepare quantum many-body systems in complex superpositions and controlling their evolution. The combination of photonic with plasmonic systems has opened up new alternatives to implement control on multiparticle quantum systems. The underlying scattering processes among photons and plasmons provide additional quantum interference paths that are of fundamental importance for controlling quantum systems. In addition, the lossy nature of plasmons offers additional mechanisms for controlling dissipative quantum dynamics through the suppression of environmental decoherence; this possibility represents one of the main goals of quantum optics. Last but not least, quantum plasmonics has unveiled the existence of exotic quantum interactions, which have extended our understanding of fundamental quantum dynamics. All of these new phenomena have triggered interests in the development of hybrid quantum networks for applications in quantum sensing, quantum metrology, quantum simulation, and information processing.

Acknowledgments: We thank the Department of Physics & Astronomy at Louisiana State University for providing startup funding, Funder Id: http://dx.doi.org/10.13039/100008294. I.D.L. acknowledges support from the Federico Baur Endowed Chair in Nanotechnology.

References

[1] Novotny L, van Hulst N. Antennas for light. Nat Photonics 2011;5:83–90.
[2] Barnes WL, Dereux A, Ebbesen TW. Surface plasmon subwavelength optics. Nature 2003;424:824–30.
[3] Ciraci C, Hill RT, Mock JJ, Urzhumov Y, et al. Probing the ultimate limits of plasmonic enhancement. Science 2012;337:1072–4.
[4] Marinica D, Kazansky A, Nordlander P, Aizpurua J, Borisov AG. Quantum plasmonics: nonlinear effects in the field enhancement of a plasmonic nanoparticle dimer. Nano Lett 2012;12:1333–9.
[5] Zapata-Herrera M, Flórez J, Camacho AS, Ramrez HY. Quantum confinement effects on the near field enhancement in metallic nanoparticles. Plasmonics 2016;13:1–7.
[6] Liedberg B, Nylander C, Lunström I. Surface plasmon resonance for gas detection and biosensing. Sens Actuators 1983;4:299–304.
[7] Cush R, Cronin J Stewart W, Maule C, Molloy J, Goddard N. The resonant mirror: a novel optical biosensor for direct sensing of biomolecular interactions. Part I: Principle of operation and associated instrumentation. Biosens Bioelectron 1993;8:347–54.
[8] Buckle P, Davies R, Kinning T, et al. The resonant mirror: a novel optical sensor for direct sensing of biomolecular interactions. Part II: applications. Biosens Bioelectron 1993;8:355–63.
[9] Cooper MA. Optical biosensors in drug discovery. Nat Rev Drug Discov 2002;1:515–28.

[10] Gramotnev DK, Bozhevolnyi SI. Nanofocusing of electromagnetic radiation. Nat Photonics 2014;8:13–22.
[11] Kauranen M, Zayats AV. Nonlinear plasmonics. Nat Photonics 2012;6:737–48.
[12] Schuller JA, Barnard ES, Cai W, Jun YC, White JS, Brongersma ML. Plasmonics for extreme light concentration and manipulation. Nat Mater 2010;9:193–204.
[13] Leon ID, Berini P. Amplification of long-range surface plasmons by a dipolar gain medium. Nat Photonics 2010;4:382–7.
[14] Berini P, Leon ID. Surface plasmon-polariton amplifiers and lasers. Nat Photonics 2011;6:16–24.
[15] Karimi E, Schulz SA, Leon ID, Qassim H, Upham J, Boyd RW. Generating optical orbital angular momentum at visible wavelengths using a plasmonic metasurface. Light Sci Appl 2014;3:e167.
[16] Ma R-M, Oulton RF, Sorger VJ, Zhang X. Plasmon lasers: coherent light source at molecular scales. Laser Photonics Rev 2013;7:1–21.
[17] Anker JN, Hall WP, Lyandres O, Shah NC, Zhao J, Van Duyne RP. Biosensing with plasmonic nanosensors. In: Nanoscience and technology: a collection of reviews from nature journals, co-published with Macmillan Publishers Ltd., UK, 2009:308–19.
[18] Leong H, Guo J. A surface plasmon resonance spectrometer using a super-period metal nanohole array. Opt Express 2012;20:21318–23.
[19] Wei J, Natelson D. Nanostructure studies of strongly correlated materials. Nanoscale 2011;3:3509–21.
[20] Tame MS, Lee C, Lee J, et al. Single-photon excitation of surface plasmon polaritons. Phys Rev Lett 2008;101:190504.
[21] Esteban R, Zugarramurdi A, Zhang P, et al. A classical treatment of optical tunneling in plasmonic gaps: extending the quantum corrected model to practical situations. Faraday Disc 2015;178:151–83.
[22] Zhu W, Esteban R, Borisov AG, et al. Quantum mechanical effects in plasmonic structures with subnanometre gaps. Nat Commun 2016;7:11495.
[23] Xu D, Xiong X, Wu L, et al. Quantum plasmonics: new opportunity in fundamental and applied photonics. Adv Opt Photonics 2018;10:703.
[24] Leon ID, Shi Z, Liapis AC, Boyd RW. Measurement of the complex nonlinear optical response of a surface plasmon-polariton. Opt Lett 2014;39:2274.
[25] Homola J. Present and future of surface plasmon resonance biosensors. Anal Bioanal Chem 2003;377:528–39.
[26] Lal S, Link S, Halas NJ. Nano-optics from sensing to waveguiding. Nat Photonics 2007;1:641–8.
[27] Chang DE, Sørensen AS, Hemmer PR, Lukin MD. Quantum optics with surface plasmons. Phys Rev Lett 2006;97:053002.
[28] Safari A, De Leon I, Mirhosseini M, Magaña Loaiza OS, Boyd RW. Light-drag enhancement by a highly dispersive rubidium vapor. Phys Rev Lett 2016;116:013601.
[29] Gao Y-P, Cao C, Duan Y-W, et al. Magnons scattering induced photonic chaos in the optomagnonic resonators. Nanophotonics 2019. Epub ahead of print.
[30] Vest B, Shlesinger I, Dheur M-C, et al. Plasmonic interferences of two-particle N00N states. N J Phys 2018;20:053050.
[31] Li D, Pacifici D. Strong amplitude and phase modulation of optical spatial coherence with surface plasmon polaritons. Sci Adv 2017;3:e1700133.
[32] Magaña-Loaiza OS, Leon ID, Mirhosseini M, et al. Exotic looped trajectories of photons in three-slit interference. Nat Commun 2016;7:13987.
[33] Safari A, Fickler R, Giese E, Magaña-Loaiza OS, Boyd RW, Leon ID. Measurement of the photon-plasmon coupling phase shift. Phys Rev Lett 2019;122:133601.
[34] Pooser RC, Lawrie B. Plasmonic trace sensing below the photon shot noise limit. ACS Photonics 2015;3:8–13.
[35] Lee C, Dieleman F, Lee J, Rockstuhl C, Maier SA, Tame M. Quantum plasmonic sensing: beyond the shot-noise and diffraction limit. ACS Photonics 2016;3:992–9.
[36] Lee J-S, Huynh T, Lee S-Y, et al. Quantum noise reduction in intensity-sensitive surface-plasmon-resonance sensors. Phys Rev A 2017;96:033833.
[37] You C, Adhikari S, Chi Y, et al. Multiparameter estimation with single photons – linearly-optically generated quantum entanglement beats the shotnoise limit. J Opt 2017;19:124002.
[38] Dowran M, Kumar A, Lawrie BJ, Pooser RC, Marino AM. Quantum-enhanced plasmonic sensing. Optica 2018;5:628.
[39] Meja-Salazar JR, Oliveira ON. Plasmonic biosensing. Chem Rev 2018;118:10617–25.
[40] Holtfrerich MW, Dowran M, Davidson R, Lawrie BJ, Pooser RC, Marino AM. Toward quantum plasmonic networks. Optica 2016;3:985.
[41] Johnson S, Dolan PR, Smith JM. Diamond photonics for distributed quantum networks. Prog Quantum Electron 2017;55:129–65.
[42] Gerry C, Knight P. Introductory quantum pptics. Cambridge University Press, 2004.
[43] Schroeter DF, Griffiths DJ. Introduction to quantum mechanics. Cambridge University Press, 2016.
[44] Scully MO, Zubairy MS. Quantum optics. Cambridge University Press, 1997.
[45] Loudon R. The quantum theory of light. Oxford University Press, 2000.
[46] Bondurant RS, Shapiro JH. Squeezed states in phase-sensing interferometers. Phys Rev D 1984;30:2548.
[47] Dowling JP. Quantum optical metrology – the lowdown on high-N00N states. Contemp Phys 2008;49:125–43.
[48] Hudelist F, Kong J, Liu C, Jing J, Ou Z, Zhang W. Quantum metrology with parametric amplifier-based photon correlation interferometers. Nat Commun 2014;5:1–6.
[49] Anisimov PM, Raterman GM, Chiruvelli A, et al. Quantum metrology with two-mode squeezed vacuum: parity detection beats the Heisenberg limit. Phys Rev Lett 2010;104:103602.
[50] Schnabel R, Mavalvala N, McClelland DE, Lam PK. Quantum metrology for gravitational wave astronomy. Nat Commun 2010;1:1–10.
[51] You C, Adhikari S, Ma X, Sasaki M, Takeoka M, Dowling JP. Conclusive precision bounds for su (1, 1) interferometers. Phys Rev A 2019;99:042122.
[52] Caves CM. Quantum-mechanical noise in an interferometer. Phys Rev D 1981;23:1693–708.
[53] Teich MC, Saleh BEA. Squeezed state of light. Quantum Opt J Eur Opt Soc Pt B 1989;1:153–91.
[54] Wu L-A, Kimble HJ, Hall JL, Wu H. Generation of squeezed states by parametric down conversion. Phys Rev Lett 1986;57:2520–3.
[55] Kumar P, Shapiro JH. Squeezed-state generation via forward degenerate four-wave mixing. Phys Rev A 1984;30:1568–71.

[56] Born M, Wolf E. Principles of optics: electromagnetic theory of propagation, interference and diffraction of light. Elsevier, 2013.
[57] Brown RH, Twiss RQ, et al. Correlation between photons in two coherent beams of light. Nature 1956;177:27–9.
[58] Knight PL. The observation of matter wave fluctuations. Science 2005;310:631–2.
[59] You C, Quiroz-Juarez MA, Lambert A, et al. Identification of light sources using artificial neural networks. arXiv preprint arXiv:1909.08060, 2019.
[60] Hong CK, Ou ZY, Mandel L. Measurement of subpicosecond time intervals between two photons by interference. Phys Rev Lett 1987;59:2044–6.
[61] Einstein A, Podolsky B, Rosen N. Can quantum-mechanical description of physical reality be considered complete? Phys Rev 1935;47:777–80.
[62] Howell JC, Bennink RS, Bentley SJ, Boyd RW. Realization of the Einstein-Podolsky-Rosen paradox using momentum- and position-entangled photons from spontaneous parametric down conversion. Phys Rev Lett 2004;92:210403.
[63] Leach J, Jack B, Romero J, et al. Quantum correlations in optical angle-orbital angular momentum variables. Science 2010;329:662–5.
[64] The BIG Bell Test Collaboration. Challenging local realism with human choices. Nature 2018;557:212.
[65] Kwiat PG, Mattle K, Weinfurter H, Zeilinger A, Sergienko AV, Shih Y. New high-intensity source of polarization-entangled photon pairs. Phys Rev Lett 1995;75:4337–41.
[66] Magaña-Loaiza OS, Boyd RW. Quantum imaging and information. Rep Prog Phys 2019;82:124401.
[67] Boyd RW. Nonlinear optics, 3rd ed. Cambridge, MA, USA, Academic Press, 2008.
[68] Horodecki R, Horodecki P, Horodecki M, Horodecki K. Quantum entanglement. Rev Mod Phys 2009;81:865–942.
[69] Maier SA. Plasmonics: fundamentals and applications. New York, NY: Springer-Verlag GmbH, 2007.
[70] Economou EN. Surface plasmons in thin films. Phys Rev 1969;182:539–54.
[71] Berini P. Long-range surface plasmon polaritons. Adv Opt Photonics 2009;1:484–588.
[72] Burke J, Stegeman G, Tamir T. Surface-polariton-like waves guided by thin, lossy metal films. Phys Rev B 1986;33:5186.
[73] Berini P. Plasmon-polariton waves guided by thin lossy metal films of finite width: bound modes of symmetric structures. Phys Rev B 2000;61:10484–503.
[74] Zia R, Selker MD, Catrysse PB, Brongersma ML. Geometries and materials for subwavelength surface plasmon modes. JOSA A 2004;21:2442.
[75] Dionne JA, Sweatlock LA, Atwater HA, Polman A. Plasmon slot waveguides: towards chip-scale propagation with subwavelength-scale localization. Phys Rev B 2006;73:035407.
[76] Jackson JD. Classical electrodynamics. John Wiley & Sons, Inc., 1998.
[77] Sönnichsen C, Franzl T, Wilk T, et al. Drastic reduction of plasmon damping in gold nanorods. Phys Rev Lett 2002;88:077402.
[78] Zentgraf T, Meyrath TP, Seidel A, et al. Babinet's principle for optical frequency metamaterials and nanoantennas. Phys Rev B 2007;76:033407.
[79] Horák M, Křápek V, Hrtoň M, et al. Limits of Babinet's principle for solid and hollow plasmonic antennas. Sci Rep 2019;9:4004.
[80] Garcia-Vidal FJ, Martin-Moreno L, Ebbesen TW, Kuipers L. Light passing through subwavelength apertures. Rev Mod Phys 2010;82:729–87.
[81] Genet C, Ebbesen TW. Light in tiny holes. In: Nanoscience and technology: a collection of reviews from nature journals, co-published with Macmillan Publishers Ltd., UK, 2009:205–12.
[82] Elson JM, Ritchie RH. Photon interactions at a rough metal surface. Phys Rev B 1971;4:4129–38.
[83] Huttner B, Barnett SM. Quantization of the electromagnetic field in dielectrics. Phys Rev A 1992;46:4306–22.
[84] Hopfield JJ. Theory of the contribution of excitons to the complex dielectric constant of crystals. Phys Rev 1958;112:1555–67.
[85] Philbin TG. Canonical quantization of macroscopic electromagnetism. N J Phys 2010;12:123008.
[86] Archambault A, Marquier F, Greffet J-J, Arnold C. Quantum theory of spontaneous and stimulated emission of surface plasmons. Phys Rev B 2010;82:035411.
[87] Waks E, Sridharan D. Cavity QED treatment of interactions between a metal nanoparticle and a dipole emitter. Phys Rev A 2010;82:043845.
[88] Dung HT, Knöll L, Welsch D-G. Three-dimensional quantization of the electromagnetic field in dispersive and absorbing inhomogeneous dielectrics. Phys Rev A 1998;57:3931–42.
[89] Trügler A, Hohenester U. Strong coupling between a metallic nanoparticle and a single molecule. Phys Rev B 2008;77:115403.
[90] Purcell EM. Spontaneous emission probabilities at radio frequencies. In: Confined electrons and photons. Springer US, 1995:839.
[91] Drexhage K, Kuhn H, Schäfer F. Variation of the fluorescence decay time of a molecule in front of a mirror. Ber Bunseng Phys Chem 1968;72:329.
[92] Chance RR, Prock A, Silbey R. Lifetime of an emitting molecule near a partially reflecting surface. J Chem Phys 1974;60:2744–8.
[93] Drexhage KH. IV interaction of light with monomolecular dye layers. Prog Opt 1974;12:163–232.
[94] Gersten J, Nitzan A. Spectroscopic properties of molecules interacting with small dielectric particles. J Chem Phys 1981;75:1139–52.
[95] Russell KJ, Liu T-L, Cui S, Hu EL. Large spontaneous emission enhancement in plasmonic nanocavities. Nat Photonics 2012;6:459–62.
[96] Kinkhabwala A, Yu Z, Fan S, Avlasevich Y, Müllen K, Moerner W. Large single-molecule fluorescence enhancements produced by a bowtie nanoantenna. Nat Photonics 2009;3:654–7.
[97] Akselrod GM, Argyropoulos C, Hoang TB, Ciracì C, Fang C, Huang J, Smith DR, Mikkelsen MH. Probing the mechanisms of large Purcell enhancement in plasmonic nanoantennas. Nat Photonics 2014;8:835–40.
[98] Schietinger S, Barth M, Aichele T, Benson O. Plasmon-enhanced single photon emission from a nanoassembled metal-diamond hybrid structure at room temperature. Nano Lett 2009;9:1694–8.
[99] Choy JT, Hausmann BJM, Babinec TM, et al. Enhanced single-photon emission from a diamond-silver aperture. Nat Photonics 2011;5:738–43.
[100] Bozhevolnyi SI, Khurgin JB. The case for quantum plasmonics. Nat Photonics 2017;11:398–400.

[101] Bozhevolnyi SI, Khurgin JB. Fundamental limitations in spontaneous emission rate of single-photon sources. Optica 2016;3:1418–21.
[102] Chikkaraddy R, De Nijs B, Benz F, et al. Single-molecule strong coupling at room temperature in plasmonic nanocavities. Nature 2016;535:127–30.
[103] Halas NJ, Lal S, Chang W-S, Link S, Nordlander P. Plasmons in strongly coupled metallic nanostructures. Chem Rev 2011;111:3913–61.
[104] Aharonovich I, Castelletto S, Simpson DA, Su C-H, Greentree AD, Prawer S. Diamond-based single-photon emitters. Rep Prog Phys 2011;74:076501.
[105] Lodahl P, Mahmoodian S, Stobbe S. Interfacing single photons and single quantum dots with photonic nanostructures. Rev Mod Phys 2015;87:347–400.
[106] Biagioni P, Huang J-S, Hecht B. Nanoantennas for visible and infrared radiation. Rep Prog Phys 2012;75:024402.
[107] Kolesov R, Grotz B, Balasubramanian G, et al. Wave-particle duality of single surface plasmon polaritons. Nat Phys 2009;5:470–4.
[108] Fuchs R, Kliewer KL. Optical properties of an electron gas: further studies of a nonlocal description. Phys Rev 1969;185:905–13.
[109] Dasgupta BB, Fuchs R. Polarizability of a small sphere including nonlocal effects. Phys Rev B 1981;24:554–61.
[110] de Abajo FJG. Nonlocal effects in the plasmons of strongly interacting nanoparticles, dimers, and waveguides. J Chem Phys C 2008;112:17983–7.
[111] David C, de Abajo FJG. Spatial nonlocality in the optical response of metal nanoparticles. J Chem Phys C 2011;115:19470–5.
[112] McMahon JM, Gray SK, Schatz GC. Nonlocal optical response of metal nanostructures with arbitrary shape. Phys Rev Lett 2009;103:097403.
[113] Raza S, Toscano G, Jauho A-P, Wubs M, Mortensen NA. Unusual resonances in nanoplasmonic structures due to nonlocal response. Phys Rev B 2011;84:121412.
[114] Toscano G, Raza S, Jauho A-P, Mortensen NA, Wubs M. Modified field enhancement and extinction by plasmonic nanowire dimers due to nonlocal response. Opt Express 2012;20:4176.
[115] Altewischer E, van Exter MP, Woerdman JP. Plasmon-assisted transmission of entangled photons. Nature 2002;418:304–6.
[116] Fasel S, Robin F, Moreno E, Erni D, Gisin N, Zbinden H. Energy-time entanglement preservation in plasmon-assisted light transmission. Phys Rev Lett 2005;94:110501.
[117] Zuloaga J, Prodan E, Nordlander P. Quantum description of the plasmon resonances of a nanoparticle dimer. Nano Lett 2009;9:887–91.
[118] Scholl JA, Garca-Etxarri A, Koh AL, Dionne JA. Observation of quantum tunneling between two plasmonic nanoparticles. Nano Lett 2013;13:564–9.
[119] Esteban R, Borisov AG, Nordlander P, Aizpurua J. Bridging quantum and classical plasmonics with a quantum-corrected model. Nat Commun 2012;3:825.
[120] Piazza L, Lummen T, Quiñonez E, et al. Simultaneous observation of the quantization and the interference pattern of a plasmonic near-field. Nat Commun 2015;6:6407.
[121] Martino GD, Sonnefraud Y, Tame M, et al. Observation of quantum interference in the plasmonic Hong-Ou-Mandel effect. Phys Rev Appl 2014;1:034004.
[122] Akimov AV, Mukherjee A, Yu CL, et al. Generation of single optical plasmons in metallic nanowires coupled to quantum dots. Nature 2007;450:402–6.
[123] Menssen AJ, Jones AE, Metcalf BJ, et al. Distinguishability and many-particle interference. Phys Rev Lett 2017;118:153603.
[124] Kawata S. Near-field optics and surface plasmon polaritons. Berlin/New York: Springer, 2001:18.
[125] Metcalf BJ, Thomas-Peter N, Spring JB, et al. Multiphoton quantum interference in a multiport integrated photonic device. Nat Commun 2013;4:1356.
[126] Zhang N, Han C, Xu Y-J, et al. Near-field dielectric scattering promotes optical absorption by platinum nanoparticles. Nat Photonics 2016;10:473–82.
[127] Vest B, Dheur M-C, Devaux É, et al. Anti-coalescence of bosons on a lossy beam splitter. Science 2017;356:1373–6.
[128] Dell'Anno F, Siena SD, Illuminati F. Multiphoton quantum optics and quantum state engineering. Phys Rep 2006;428:53–168.
[129] O'Brien JL, Furusawa A, Vučković J. Photonic quantum technologies. Nat Photonics 2009;3:687–95.
[130] Aspuru-Guzik A, Walther P. Photonic quantum simulators. Nat Phys 2012;8:285–91.
[131] Spring JB, Metcalf BJ, Humphreys PC, et al. Boson sampling on a photonic chip. Science 2012;339:798–801.
[132] Peruzzo A, McClean J, Shadbolt P, et al. A variational eigenvalue solver on a photonic quantum processor. Nat Commun 2014;5:4213.
[133] Wang H, He Y, Li Y-H, et al. High-efficiency multiphoton boson sampling. Nat Photonics 2017;11:361–5.
[134] Schouten HF, Kuzmin N, Dubois G, et al. Plasmon-assisted two-slit transmission: Young's experiment revisited. Phys Rev Lett 2005;94:053901.
[135] Iskhakov TS, Chekhova MV, Rytikov GO, Leuchs G. Macroscopic pure state of light free of polarization noise. Phys Rev Lett 2011;106:113602.
[136] Fasel S, Halder M, Gisin N, Zbinden H. Quantum superposition and entanglement of mesoscopic plasmons. N J Phys 2006;8:13.
[137] Huck A, Smolka S, Lodahl P, et al. Demonstration of quadrature-squeezed surface plasmons in a gold waveguide. Phys Rev Lett 2009;102:246802.
[138] Martino GD, Sonnefraud Y, Kéna-Cohen S, et al. Quantum statistics of surface plasmon polaritons in metallic stripe waveguides. Nano Lett 2012;12:2504–8.
[139] Ren XF, Guo GP, Huang YF, Li CF, Guo GC. Plasmon-assisted transmission of high-dimensional orbital angular-momentum entangled state. EPL Europhys Lett 2006;76:753–9.
[140] Guo G-P, Ren X-F, Huang Y-F, Li C-F, Ou Z-Y, Guo G-C. Observation of two-photon coherence in plasmon-assisted transmission. Phys Lett A 2007;361:218–22.
[141] Fujii G, Segawa T, Mori S, Namekata N, Fukuda D, Inoue S. Preservation of photon indistinguishability after transmission through surface-plasmon-polariton waveguide. Opt Lett 2012;37:1535.
[142] Jabir MV, Chaitanya NA, Aadhi A, Samanta GK. Generation of "perfect" vortex of variable size and its effect in angular spectrum of the down-converted photons. Sci Rep 2016;6:21877.

[143] Jabir MV, Chaitanya NA, Mathew M, Samanta GK. Direct transfer of classical non-separable states into hybrid entangled two photon states. Sci Rep 2017;7:7331.
[144] Jabir MV, Samanta GK. Robust, high brightness, degenerate entangled photon source at room temperature. Sci Rep 2017;7:12613.
[145] Wang H, Qin J, Ding X, et al. Boson sampling with 20 input photons and a 60-mode interferometer in a 10^{14}-dimensional Hilbert space. Phys Rev Lett 2019;123:250503.
[146] Harder G, Bartley TJ, Lita AE, Nam SW, Gerrits T, Silberhorn C. Single-mode parametric-down-conversion states with 50 photons as a source for mesoscopic quantum optics. Phys Rev Lett 2016;116:143601.
[147] Magaña-Loaiza OS, de León-Montiel RJ, Perez-Leija A, et al. Multiphoton quantum-state engineering using conditional measurements. npj Quantum Inf 2019;5:80.
[148] Tichy MC, Tiersch M, Mintert F, Buchleitner A. Many-particle interference beyond many-boson and many-fermion statistics. N J Phys 2012;14:093015.
[149] Spagnolo N, Vitelli C, Aparo L, et al. Three-photon bosonic coalescence in an integrated tritter. Nat Commun 2013;4:1606.
[150] Dheur M-C, Devaux E, Ebbesen TW, et al. Single-plasmon interferences. Sci Adv 2016;2:e1501574.
[151] Heeres RW, Kouwenhoven LP, Zwiller V. Quantum interference in plasmonic circuits. Nat Nanotechnol 2013;8:719–22.
[152] Fakonas JS, Lee H, Kelaita YA, Atwater HA. Two-plasmon quantum interference. Nat Photonics 2014;8:317–20.
[153] Cai Y-J, Li M, Ren X-F, et al. High-visibility on-chip quantum interference of single surface plasmons. Phys Rev Appl 2014;2:014004.
[154] Fujii G, Fukuda D, Inoue S. Direct observation of bosonic quantum interference of surface plasmon polaritons using photon-number-resolving detectors. Phys Rev B 2014;90:085430.
[155] Daniel S, Saastamoinen K, Saastamoinen T, Vartiainen I, Friberg AT, Visser TD. Surface plasmons carry the Pancharatnam-Berry geometric phase. Phys Rev Lett 2017;119:253901.
[156] Berry MV. Quantal phase factors accompanying adiabatic changes. Proc R Soc A Math Phys Eng Sci 1984;392:45–57.
[157] Kolobov MI. Quantum imaging. New York: Springer, 2006.
[158] Lugiato LA, Gatti A, Brambilla E. Quantum imaging. J Opt B Quantum Semiclassic Opt 2002;4:S176–83.
[159] Glasser RT, Cable H, Dowling JP, Martini FD, Sciarrino F, Vitelli C. Entanglement-seeded, dual, optical parametric amplification: applications to quantum imaging and metrology. Phys Rev A 2008;78:012339.
[160] Abouraddy AF, Saleh BEA, Sergienko AV, Teich MC. Role of entanglement in two-photon imaging. Phys Rev Lett 2001;87:123602.
[161] Curty M, Lewenstein M, Lütkenhaus N. Entanglement as a precondition for secure quantum key distribution. Phys Rev Lett 2004;92:217903.
[162] Silberhorn C, Korolkova N, Leuchs G. Quantum key distribution with bright entangled beams. Phys Rev Lett 2002;88:167902.
[163] Jennewein T, Simon C, Weihs G, Weinfurter H, Zeilinger A. Quantum cryptography with entangled photons. Phys Rev Lett 2000;84:4729–32.
[164] Ma X, Fung C-HF, Lo H-K. Quantum key distribution with entangled photon sources. Phys Rev A 2007;76:012307.
[165] Tsujimoto Y, You C, Wakui K, et al. Heralded amplification of nonlocality via entanglement swapping. N J Phys 2019;22:023008.
[166] Penrose R. Quantum computation, entanglement and state reduction. Philos Trans R Soc Lond Ser A Math Phys Eng Sci 1998;356:1927–39.
[167] Jozsa R, Linden N. On the role of entanglement in quantum-computational speed-up. Philos Trans R Soc Lond Ser A Math Phys Eng Sci 2003;459:2011–32.
[168] Preskill J. Quantum computing and the entanglement frontier. arXiv preprint arXiv:1203.5813, 2012.
[169] Karlsson A, Koashi M, Imoto N. Quantum entanglement for secret sharing and secret splitting. Phys Rev A 1999;59:162–8.
[170] Ursin R, Tiefenbacher F, Schmitt-Manderbach T, et al. Entanglement-based quantum communication over 144km. Nat Phys 2007;3:481.
[171] Tame MS, McEnery KR, Özdemir SK, Lee J, Maier SA, Kim MS. Quantum plasmonics. Nat Phys 2013;9:329–40.
[172] Zhou Z-K, Liu J, Bao Y, et al. Quantum plasmonics get applied. Prog Quantum Electron 2019;65:1–20.
[173] Moreno E, Garca-Vidal FJ, Erni D, Cirac JI, Martin-Moreno L. Theory of plasmon-assisted transmission of entangled photons. Phys Rev Lett 2004;92:236801.
[174] van Velsen JL, Tworzydło J, Beenakker CWJ. Scattering theory of plasmon-assisted entanglement transfer and distillation. Phys Rev A 2003;68:043807.
[175] Dieleman F, Tame MS, Sonnefraud Y, Kim MS, Maier SA. Experimental verification of entanglement generated in a plasmonic system. Nano Lett 2017;17:7455–61.
[176] Fakonas JS, Mitskovets A, Atwater HA. Path entanglement of surface plasmons. N J Phys 2015;17:023002.
[177] Asano M, Bechu M, Tame M, et al. Distillation of photon entanglement using a plasmonic metamaterial. Sci Rep 2015;5:18313.
[178] Li M, Zou C-L, Ren X-F, et al. Transmission of photonic quantum polarization entanglement in a nanoscale hybrid plasmonic waveguide. Nano Lett 2015;15:2380–4.
[179] Chen Y, Lee C, Lu L, et al. Quantum plasmonic n00n state in a silver nanowire and its use for quantum sensing. Optica 2018;5:1229–35.
[180] Büse A, Juan ML, Tischler N, et al. Symmetry protection of photonic entanglement in the interaction with a single nanoaperture. Phys Rev Lett 2018;121:173901.
[181] Tischler N, Rockstuhl C, Słowik K. Quantum optical realization of arbitrary linear transformations allowing for loss and gain. Phys Rev X 2018;8:021017.
[182] Xiao Z, Lanning RN, Zhang M, Novikova I, Mikhailov EE, Dowling JP. Why a hole is like a beam splitter: a general diffraction theory for multimode quantum states of light. Phys Rev A 2017;96:023829.
[183] Harris SE, Yamamoto Y. Photon switching by quantum interference. Phys Rev Lett 1998;81:3611–4.
[184] Jung J, Søndergaard T, Bozhevolnyi SI. Theoretical analysis of square surface plasmon-polariton waveguides for long-range polarization-independent waveguiding. Phys Rev B 2007;76:035434.
[185] de Leon NP, Lukin MD, Park H. Quantum plasmonic circuits. IEEE J Sel Top Quantum Electron 2012;18:1781–91.
[186] Davis TJ, Gómez DE, Roberts A. Plasmonic circuits for manipulating optical information. Nanophotonics 2016;6.

[187] Wang K, Titchener JG, Kruk SS, et al. Quantum metasurface for multiphoton interference and state reconstruction. Science 2018;361:1104–8.
[188] Taballione C, Wolterink TAW, Lugani J, et al. 8×8 reconfigurable quantum photonic processor based on silicon nitride waveguides. Opt Express 2019;27:26842.
[189] Wang SM, Cheng QQ, Gong YX, et al. A $14\times14um^2$ footprint polarization-encoded quantum controlled-NOT gate based on hybrid waveguide. Nat Commun 2016;7:11490.
[190] Carminati R, Greffet J-J. Near-field effects in spatial coherence of thermal sources. Phys Rev Lett 1999;82:1660–3.
[191] Gan CH, Gbur G, Visser TD. Surface plasmons modulate the spatial coherence of light in young's interference experiment. Phys Rev Lett 2007;98:043908.
[192] Gan CH, Gu Y, Visser TD, Gbur G. Coherence converting plasmonic hole arrays. Plasmonics 2012;7:313–22.
[193] Kuzmin N, Hooft GW't, Eliel ER, Gbur G, Schouten HF, Visser TD. Enhancement of spatial coherence by surface plasmons. Opt Lett 2007;32:445–7.
[194] Ravets S, Rodier JC, Kim BE, Hugonin JP, Jacubowiez L, Lalanne P. Surface plasmons in the young slit doublet experiment. JOSA B 2009;26:B28.
[195] Divitt S, Frimmer M, Visser TD, Novotny L. Modulation of optical spatial coherence by surface plasmon polaritons. Opt Lett 2016;41:3094.
[196] Sawant R, Samuel J, Sinha A, Sinha S, Sinha U. Nonclassical paths in quantum interference experiments. Phys Rev Lett 2014;113:120406.